

## Responsibility of a Filament Eruption for the Initiation of a Flare, CME, and Blast Wave, and its Possible Transformation into a Bow Shock

V.V. Grechnev<sup>1</sup> · A.M. Uralov<sup>1</sup> ·  
I.V. Kuzmenko<sup>2</sup> · A.A. Kochanov<sup>1</sup> ·  
I.M. Chertok<sup>3</sup> · S.S. Kalashnikov<sup>1</sup>

Received ; accepted

© Springer ●●●

### Abstract

Multi-instrument observations of two filament eruptions on 24 February and 11 May 2011 suggest the following updated scenario for eruptive flare, CME and shock wave evolution. An initial destabilization of a filament results in stretching out of magnetic threads belonging to its body and rooted in the photosphere along the inversion line. Their reconnection leads to i) heating of parts of the filament or its environment, ii) initial development of the flare arcade cusp and ribbons, and iii) increasing similarity of the filament to a curved flux rope and its acceleration. Then the pre-eruption arcade enveloping the filament gets involved in reconnection according to the standard model and continues to form the flare arcade and ribbons. The poloidal magnetic flux in the curved rope developing from the filament progressively increases and forces its toroidal expansion. This flux rope impulsively expands and produces an MHD disturbance, which rapidly steepens into a shock. The shock passes through the arcade expanding above the filament and then freely propagates ahead of the CME like a decelerating blast wave for some time. If the CME is slow, then the shock eventually decays. Otherwise, the frontal part of the shock changes into the bow-shock regime. This was observed for the first time in the 24 February 2011 event. When reconnection ceases, the flux rope relaxes and constitutes the CME core–cavity system. The expanding arcade develops into the CME frontal structure. We also found that reconnection in the current sheet of a remote streamer forced by the shock’s passage results in a running flare-like process within the streamer responsible for

---

<sup>1</sup> Institute of Solar-Terrestrial Physics SB RAS, Lermontov St. 126A, Irkutsk 664033, Russia email: grechnev@iszf.irk.ru email: uralov@iszf.irk.ru email: kochanov@iszf.irk.ru

<sup>2</sup> Ussuriysk Astrophysical Observatory, Solnechnaya St. 21, Primorsky Krai, Gornotaezhnoe 692533, Russia email: kuzmenko\_irina@mail.ru

<sup>3</sup> Pushkov Institute of Terrestrial Magnetism, Ionosphere and Radio Wave Propagation (IZMIRAN), Troitsk, Moscow, 142190 Russia email: ichertok@izmiran.ru

a type II burst. The development of dimming and various associated phenomena are discussed.

**Keywords:** Filament Eruptions; Flares; Coronal Mass Ejections; Shock Waves; Type II Bursts

*Dedicated to the memory of Mukul Kundu who  
inspired a significant part of our study*

## 1. Introduction

### 1.1. Challenges of Solar Eruptions

The causes of solar flares, their relations to filament eruptions, coronal mass ejections (CMEs), and underlying processes have been considered for several decades. A number of flare models have been proposed. The ‘standard’ flare model, referred to as ‘CSHKP’ for its contributors (Carmichael, 1964; Sturrock, 1966; Hirayama, 1974; Kopp and Pneuman, 1976), is the most elaborated one, being extensively supported by observations. In particular, Hirayama (1974) proposed that the current sheet, in which the flare reconnection occurred, formed due to the lift-off of a filament, whose eruption was driven by a magnetohydrodynamic (MHD) instability of an increasing current in the filament. This scenario directly associated a flare with an eruption, and thus provided a basis for understanding the initiation of CMEs. Later considerations adopted the scenario of Hirayama (1974), but the filaments (prominences) were mainly assumed to be passive dense plasmas accumulated near the bottom of eruptive flux ropes. This picture revealed from non-flare-related eruptions of filaments outside of active regions (ARs), is thought to also apply to the flare-related eruptions from ARs. However, the causes of the eruptions themselves have not been elaborated by the standard model; and the model did not incorporate confined flares.

The idea of Hirayama (1974) was elaborated by Chen (1989, 1996), who developed a theory of the expansion of a magnetic flux rope. The propelling force driving an eruption in the Chen’s *Flux rope model* is the Lorentz force, which governs the torus instability. The difficulty of this model is that the ongoing injection of the poloidal magnetic flux is required to ensure the expansion of a CME (Krall, Chen, and Santoro, 2000). The *Breakout* reconnection (Antiochos, DeVore, and Klimchuk, 1999; Lynch *et al.*, 2008) can help to overcome the magnetic tension of the transverse magnetic flux above the rope.

Another model of eruptions, the *Tether cutting model* proposed by Moore *et al.* (2001), is currently popular. A case study of an eruptive event lead Sterling, Moore, and Thompson (2001) to a conclusion that the ‘tether cutting’ reconnection occurred after the eruption onset only as a by-product, while this scenario might apply to different events.

Inhester, Birn, and Hesse (1992) proposed the formation of the poloidal magnetic flux due to reconnection in a sheared arcade, based on the original idea of van Ballegoijen and Martens (1989) (*cf.* Uralov, 1990a, 1990b). This scenario (see also Longcope and Beveridge, 2007) was confirmed quantitatively in the

comparison of the magnetic flux reconnected in flares with the poloidal flux of the corresponding magnetic clouds near Earth (Qiu *et al.*, 2007). Zhang *et al.* (2001) and Temmer *et al.* (2008, 2010) found a temporal correspondence between the hard X-ray flare emission and acceleration of a CME. This fact is considered as a further support to the formation of the CME’s poloidal flux in the course of magnetic reconnection responsible for the corresponding flare.

The *dual-filament model* (Uralov *et al.*, 2002; Grechnev *et al.*, 2006) combines the processes employed by the standard model with effects of joining two filaments. The increased total twist in the combined filament forces the development of the torus instability. The combination of the backbone fields of the filaments creates the initial propelling force. These processes induce the stretching the numerous filament threads anchored in the photosphere and reconnection between them, thus increasing the inner twist. Reconnection in the enveloping arcade augments the outer twist, as in the standard model. The formerly stable filament transforms into a ‘mainspring’.

This brief overview shows that many years of observational and theoretical studies of solar eruptions have not yet led to consensus about their scenarios, relation to flares, and the development of CMEs. It is possible that different scenarios adequately describe the events of different types. Observational limitations restricted the opportunities to verify the existing concepts.

## 1.2. Excitation of Shock Waves

Another subject of long-standing debates is related to shock waves propagating in the corona. Their existence is evidenced by several phenomena. Following Uchida (1968), Moreton waves are considered as lower skirts of coronal shock waves. Many ‘EUV waves’ are also candidates. Type II radio bursts and interplanetary shocks provide further support. Nevertheless, the origin of shocks remains controversial (see, *e.g.*, Vršnak and Cliver, 2008 for a review).

The first historical concept ascribed the excitation of coronal shock waves to the flare plasma pressure pulses. In the scenario of Hirayama (1974), ‘*in front of the prominence a shock wave may be generated and this might be the cause of either type-II or moving type-IV burst*’. A popular scenario favored by the *in situ* observations of bow shocks ahead of interplanetary CMEs (ICMEs) and studies of solar data (Cliver *et al.*, 2004) relates the excitation of ‘CME-driven shocks’ to the outer surfaces of super-Alfvénic CMEs.

Grechnev *et al.* (2011b, 2011a, 2013, 2014a) argued in favor of the shock wave excitation by impulsively erupting flux ropes, similar to the conjecture of Hirayama (1974). A flux rope forming from the filament, initially located low in the corona, sharply accelerates and produces an MHD disturbance. It rapidly steepens into a shock above an AR, where the fast-mode speed steeply falls off (Afanasyev, Uralov, and Grechnev, 2013), and then freely propagates like a decelerating blast wave. One might expect that such blast-wave-like shocks propagating ahead of CMEs either eventually get transformed into bow shocks, if the CME is fast, or decay into a weak disturbance otherwise.

### 1.3. Data, Approaches, and Aims

The uncertainties in the scenarios of eruptions, CMEs, and excitation of shocks are due to the limitations of observations. Ground-based observations of eruptions carried out mostly in the H $\alpha$  line are restricted by the loss of the opacity of eruptions in their expansion, and the Doppler shift removing them from the filter passband. Space-borne observations in the He II 304 Å line, which is well-suited for the detection of prominences, were infrequent in the past. The loss of the LASCO/C1 coronagraph on SOHO in 1998 resulted in a large gap between the observations of near-surface activity and white-light CMEs. SOHO/EIT provided insufficient temporal sampling of eruptions and wave-like disturbances. Multi-wavelength data of a high temporal and spatial resolution from telescopes of modern space missions such as the *Sun Earth Connection Coronal and Heliospheric Investigation* instrument suites (SECCHI; Howard *et al.*, 2008) on the twin-spacecraft *Solar-Terrestrial Relations Observatory* (STEREO; Kaiser *et al.*, 2008), the *Atmospheric Imaging Assembly* (AIA) on the *Solar Dynamics Observatory* (SDO; Lemen *et al.*, 2012) crucially improve the situation.

An important contribution is provided by observations of radio emission. It is generated by various mechanisms and carries quantitative information about them. Microwave images show filaments and prominences with a large field of view, which can overlap with the images produced by the SOHO's *Large Angle and Spectroscopic Coronagraph* (LASCO; Brueckner *et al.*, 1995). Microwave images from the *Nobeyama Radioheliograph* (NoRH; Nakajima *et al.*, 1994) and *Siberian Solar Radio Telescope* (SSRT; Smolkov *et al.*, 1986; Grechnev *et al.*, 2003) have been successfully used in studies of eruptions and related phenomena (*e.g.*, Hanaoka *et al.*, 1994; Uralov *et al.*, 2002; Shimojo *et al.*, 2006; Grechnev *et al.*, 2006, 2008; Alissandrakis *et al.*, 2013). The dynamic radio spectra reveal the signatures of propagating shocks (type IIs) and expanding ejecta (type IVs).

Measurements of eruptive features, which are usually faint relative to associated flares, are complicated by a rapid decrease of their brightness or opacity. The difficulties to detect and follow them in all analyzed images lead to large positional uncertainties. Even in modern elaborations (*e.g.*, Vršnak *et al.*, 2007; Temmer *et al.*, 2010), the differentiation of the measured distance-time points causes a large scatter of the velocities and accelerations. This drawback is reduced in the approach based on the fit of an analytic function to the measurements (*e.g.*, Gallagher, Lawrence, and Dennis, 2003; Sheeley, Warren, and Wang, 2007; Wang, Zhang, and Shen, 2009; Alissandrakis *et al.*, 2013). The approach uses the fact that the initial and final velocities of an eruption are nearly constant, while the acceleration occurs within a limited time interval. We fit the acceleration with a Gaussian time profile. The kinematical plots are calculated by means of the integration of the analytic fit rather than the differentiation of the measurements. The results of the fit are used as a starting estimate of the parameters of the acceleration, and then they are optimized to outline the eruption in a best way. Our ultimate criterion is to follow the analyzed feature as closely as possible in all of the images. If the kinematics is more complex, then we use a combination of Gaussians and adjust their parameters manually. The major errors are due to the uncertainties in following a moving feature, whose

visibility decreases. All methods should converge to similar results. The accuracy and performance of each method are different. The accuracy is essential for our purposes.

Our measurements of wave signatures are based on the same approach and a power-law fit expected for shock waves. The techniques are described in Grechnev *et al.* (2011b, 2011a, 2013, 2014b, 2014a).

Using multi-instrument observations in various spectral ranges, we pursue a deeper insight into the following issues: how do impulsive eruptions occur; how do CMEs form; when and where are shock waves excited, and where they in the images are; are they related to ‘EUV waves’ or not. For these purposes we consider two eruptive events of different energetics. We analyze the observed relations between the filament eruptions and the onset of the flares. To reveal the histories of the disturbances produced by the eruptions, we detect and reconcile their manifestations at different wavelengths such as the response of individual coronal structures located not far from the eruption sites; large-scale ‘EUV waves’; the outermost envelopes of the white-light CMEs; the trajectories and structures of type II radio bursts.

Section 2 addresses a strong event responsible for a blast-wave-like shock, which then approached the bow-shock regime. Section 3 considers the development of a CME in a weak event, also responsible for a blast-wave-like shock, which decayed into a weak disturbance. The results are discussed in Section 4 and summarized in Section 5. The events and the measurements are illustrated by the movies accompanying the electronic version of the paper.

## 2. Event I: 24 February 2011

A prominence eruption associated with an M3.5 flare occurred on 24 February 2011 around 07:30 (*all times hereafter refer to UT*) on the east limb. The event was observed along the Sun–Earth line by SDO/AIA, SOHO/LASCO, and the *Reuven Ramaty High-Energy Solar Spectroscopic Imager* (RHESSI; Lin *et al.*, 2002). The eruption site were also visible from STEREO-B, which was located  $94^{\circ}.55$  east of the Earth at a distance of 1.022 AU from the Sun.

The eruption was analyzed by Kumar *et al.* (2012), who concluded that the prominence accelerated due to the torus instability. Considering in terms of high-beta conditions the role of the plasma pressure in the initiation of the eruption, the authors have not come to a certain conclusion because of the unknown plasma density and magnetic field strength in the prominence, which was supposed to be a part of a larger flux rope. We will address the kinematics of the eruptive structures, their relation to the flare, and follow the development of the shock wave and CME.

### 2.1. Filament Eruption

The initiation phase manifested in gradual changes of the V-shaped filament visible in STEREO-B/EUVI 304 Å images more than half an hour before the eruption. In Figure 1a, the axis of the west filament arm is traced with the

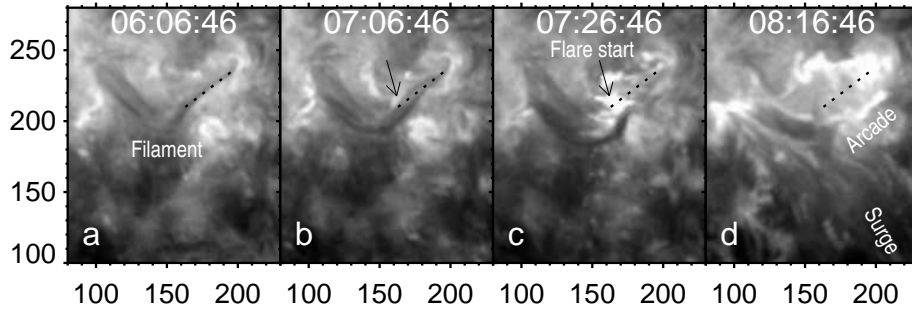


**Figure 1.** The eruption region of the 24 February 2011 event observed with STEREO-B/EUVI in 304 Å: (a), (b) initiation, (c) the onset of the eruption and flare, (d) post-eruption arcade. The images were rotated to 07:30. The black dotted bar marks the initial axis of the west filament arm. The arrows in panels (b) and (c) indicate the appearing flare brightening. The field of view corresponds to the red frame in Figure 7a. The axes show arc seconds from the solar disk center.

dotted bar. No indications of a helical structure are pronounced. In Figure 1b, the filament slightly straightened and broadened. A small region indicated by the arrow started to brighten up. In Figure 1c, the filament is considerably displaced. The flare brightening became conspicuous. Its rhombus-like extensions were due to an overexposure distortion, which contaminated the images during the flare. Figure 1d shows a post-eruption arcade and a surge emanating from the east filament toward the southwest. The axis of the west arcade portion was close to that of the pre-eruption filament, in agreement with the CSHKP model.

The activation of the filament was accompanied by a gradual rise of the soft X-ray (SXR) flux in Figures 2a and Figure 2b. This observation supports and elaborates the conjecture of Zhang *et al.* (2001) about the correspondence between the activation of a filament and a gradual rise of the SXR flux.

The filament started to erupt at about 07:27 and separated (see the movies 20110224\_euvi\_304\_fulldisk.mpg and 20110224\_euvi\_195\_fulldisk.mpg). Its fastest portion is detectable in the 304 Å image ratio at 08:06:46 above the southwest limb at  $-45^\circ$  from the west direction, along the axis of AR 11164 (the arrow in Figure 7). We adopt this angle as the initial orientation of the CME in the plane of the sky of STEREO-B. This eruption moved perpendicularly to a presumable arrangement of the streamer belt near this part of the limb.

The flare site at a longitude of E84 was visible from the Earth. Thus, RHESSI data provide complete information about hard X-ray (HXR) emission of this flare (Battaglia and Kontar, 2012; Martínez-Oliveros *et al.*, 2012). Figure 2d presents the HXR burst in two energy bands in comparison with the derivatives of two GOES channels in Figure 2c. The Neupert effect (Neupert, 1968) worked well, being somewhat energy dependent. This fact confirms the simple scenario with chromospheric evaporation caused by precipitating electrons and confinement of evaporated plasmas in the flare loops emitting soft X-rays (Kumar *et al.*, 2012), unlike the events with more than one eruption, when pronounced deviations from the Neupert effect can occur (see, *e.g.*, Grechnev *et al.*, 2013).

The detailed AIA data present a violent prominence eruption (see also the movie 20110224\_AIA\_211\_eruption.mpg). Figure 3 shows eight pairs of the AIA

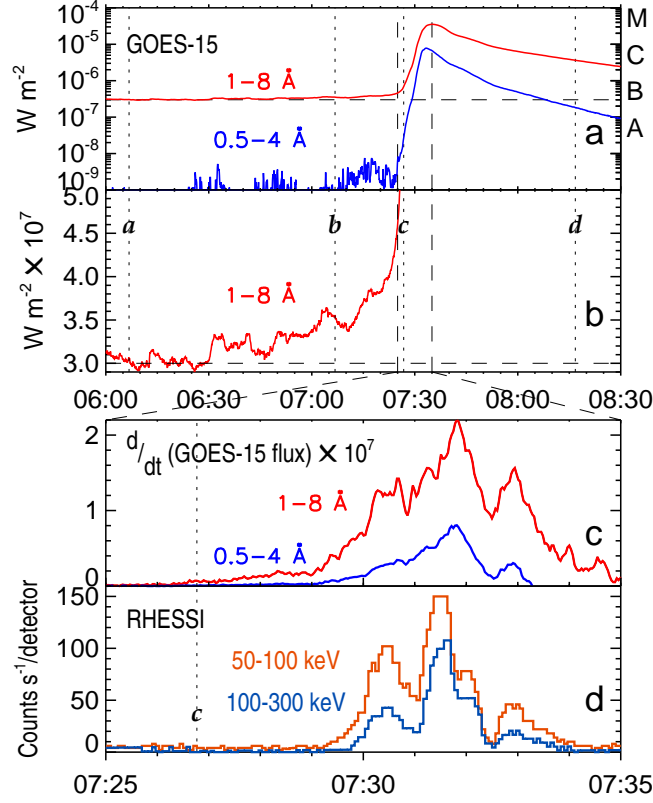


**Figure 2.** GOES time profiles of the SXR emission in the 24 February 2011 event in the logarithmic (a) and linear (b) scales, (c) their derivatives, and (d) hard X-ray burst recorded with RHESSI. The dotted vertical lines mark the observation times of the images in Figure 1. The dashed vertical lines in panels a) and b) mark the interval shown in panels (c) and (d).

211 Å images (the characteristic temperature is 2 MK). The left panel in each pair presents a 211 Å image in the logarithmic brightness scale; the right panel presents a running-difference ratio of the left image to the pre-event one. The structure in the figure looks like the cross section of a large flux rope, whose axis had an acute angle with the line of sight, and passive prominence material in its bottom part. However, the picture revealed by the AIA data is more complex.

Initially, the prominence was dark and screened features behind it such as a bright ring in Figure 3c. This fact indicates absorption, which occurs if the temperature of the prominence body is low,  $\lesssim 10^4$  K (see, *e.g.*, Grechnev *et al.*, 2008, 2014b). Then a helical structure of the prominence appeared and evolved. The small ring became bright at 211 Å that indicates its heating up to  $\gtrsim 2$  MK (or still higher, see Kumar *et al.*, 2012). The brightening of the formerly dark prominence suggests an increase of the plasma pressure,  $2nkT$ , by a factor of  $\gtrsim 200$  (*cf.* Grechnev *et al.*, 2014b). Such a strong pressure rise could deform the prominence and inspire the development of some instability. The rise of the SXR flux during the initiation phase supports the role of heating.



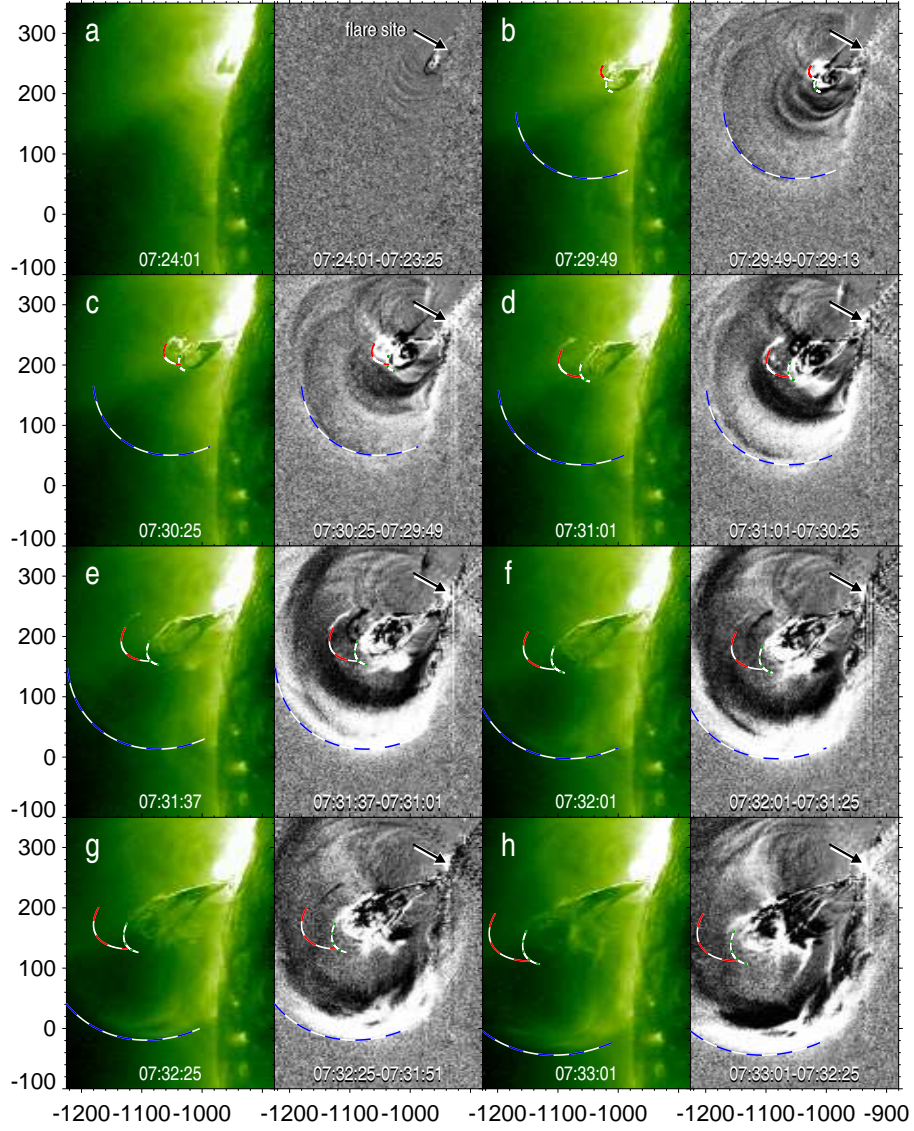


**Figure 3.** Prominence eruption on 24 February 2011 observed by SDO/AIA in 211 Å. The left, green panel of each pair of the images from (a) to (h) presents an enhanced-contrast image, and each right, gray-scale panel shows a running-difference ratio. The dashed arcs outline the bright (red/white) and dark (green/white) rings of the eruptive prominence and the overlying arcade loop (blue/white) according to the kinematic measurements in Figure 4. The arrow in the right panels indicates the flare site. The axes show the coordinates in arcsec from the solar disk center.



The gray-scale right panels of Figure 3 show concentric loops of a pre-eruption arcade. The loops embraced the prominence; their expansion lagged behind it. Figures 4a–4c present the kinematics of two prominence segments and one of the outermost loops, whose delay is most pronounced. The measurement technique (Grechnev *et al.* 2011b, 2014b) is briefly described in Section 1.3. The errors of  $\pm 15''$  produce minor uncertainties in the velocities of the filament segments of  $\pm 4\%$  and acceleration center times of  $\pm 9$  s. The acceleration of the arcade is more uncertain. Applying to the arcade loop a much shorter, stronger acceleration with the same center time results in an indiscernible change of the calculated positions. Therefore, the solid blue plots for the loop in Figures 4a and 4b are the limits corresponding to the longest acceleration. The dashed blue curves correspond to a shorter acceleration time. The measurements are limited by the field of view of AIA; the final speeds of the eruptive features can be higher.

The eruption in Figure 3 moved with an angle of  $\approx 25^\circ$  to the east direction visible from SDO. Its orientation with respect to the west direction visible from STEREO-B was  $\approx 45^\circ$  (Figure 7). Using the nearly perpendicular viewing direction of STEREO-B relative to the Sun–Earth line, one can approximately estimate the velocity components directly from the images observed with STEREO-B and AIA: the module of the velocity and acceleration vectors should be related to the plane-of-the-sky measurements from AIA data by a factor of about 1.09.

The bright helical ring of the eruptive prominence was a most dynamic feature, leading all others. Its acceleration was the highest one and reached  $a_{1(\text{POS})} \approx 13 \text{ km s}^{-2}$  in the plane of the sky ( $|\mathbf{a}_1| \approx 14 \text{ km s}^{-2} \approx 50g_\odot$ ;  $g_\odot = 274 \text{ m s}^{-2}$  is the solar gravity acceleration at the photospheric level). The darker ring accelerated somewhat later with  $a_{2(\text{POS})} \approx 5 \text{ km s}^{-2}$ . The prominence drove the expansion of the arcade, which lagged behind the fastest prominence ring by about 1.5 min.

It is useful to compare the acceleration of the eruption with the bursts in HXR (RHESSI) and microwaves (USAF RSTN San Vito and Learmonth stations). The correspondence between HXR and microwave bursts is well known. A temporal correspondence between HXR bursts and CME acceleration was established by Temmer *et al.* (2008, 2010). Here we see that the latter correspondence might be due to the delays of both the arcade expansion and flare emission with respect to the acceleration of the prominence, which itself could be the developing flux rope. The prominence threads in Figure 3 were connected to the flare site resembling a flare cusp. The dynamic cusp formation was previously considered by Sui, Holman, and Dennis (2008). The distance between the cusp and the flare site was  $\lesssim 50$  Mm. The delayed flare development relative to the eruption agrees with the standard model. The observations do not reveal any signs of the break-out reconnection (Antiochos, DeVore, and Klimchuk, 1999) within the field of view of AIA; the eruptive prominence apparently had to overcome the magnetic tension of the overlying closed fields by itself. Neither the images in Figure 3 show the lateral overexpansion discussed by Patsourakos, Vourlidas, and Stenborg (2010). The shape of the arcade looks consistent with a limitation of its expansion by the solar surface and a tilted motion of the eruptive prominence.

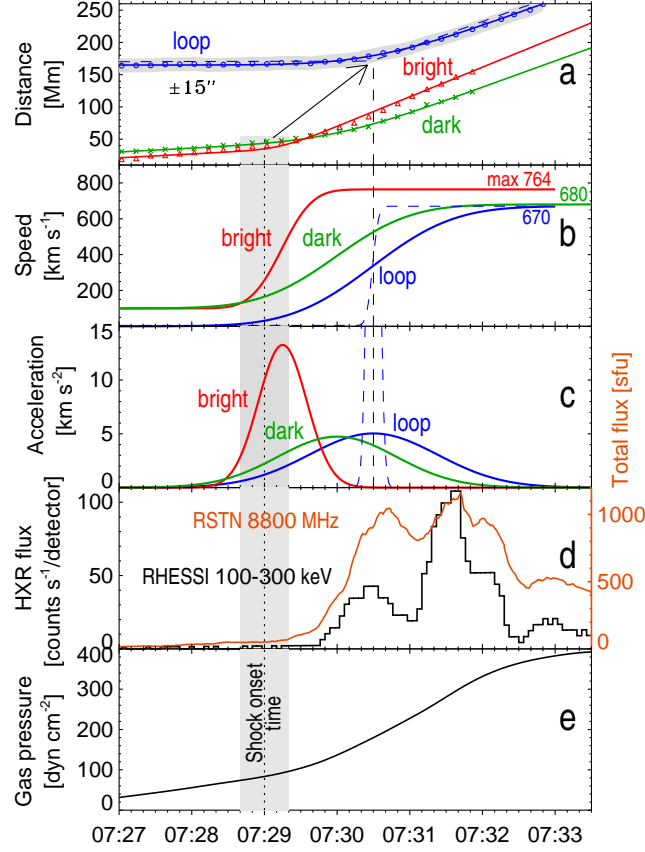


**Figure 4.** Plane-of-the-sky kinematics of the eruptive prominence and enveloping arcade measured from AIA images (a–c) in comparison with HXR and microwave time profiles (d), and gas pressure in flare loops (e). The symbols in panel (a) represent the coarse starting measurements, and the gray error band corresponds to  $\pm 15''$ . The blue dashed lines schematically show the plots for a possible shorter acceleration of the arcade loop. The dotted vertical line denotes the estimated shock onset time, and the shaded interval presents its uncertainty. The dashed vertical line corresponds to the acceleration center time of the arcade. The arrow in panel (a) indicates a disturbance propagating from the erupting prominence to the arcade. The tilt of the arrow corresponds to the average speed of the disturbance of  $\approx 1500 \text{ km s}^{-1}$  within the time interval between the ends of the arrow.

Figure 4e presents the evolution of the plasma pressure in flare loops computed from SXR GOES fluxes. The temperature,  $T$ , and emission measure, EM, were calculated from the SXR fluxes by means of the standard GOES software. The number density,  $n$ , was estimated as  $n = \sqrt{\text{EM}/V}$ , with a volume  $V \approx A^{3/2}$ . To find the area,  $A$ , we used the dimensions of the SXR-emitting source evaluated by Battaglia and Kontar (2012) from RHESSI images. The pressure,  $2nkT$ , steadily rose until a maximum at 07:33:44, and then started to gradually decrease. The half-height duration of the gradual pressure pulse was about 18 min. These characteristics of the flare pressure rule out its significance in the initiation of either the eruption or the wave, whose estimated onset time,  $t_0 \approx 07:29:00$ , is marked in Figure 4 with the dotted line. A similar relation between the wave onset and

flare pressure was shown for different events by Grechnev *et al.* (2011b). They also presented the reasons why the flare-ignition of shocks is not expected, in general.

The eruptive prominence underwent an impulsive acceleration up to  $|\mathbf{a}| \approx 50g_{\odot}$ . This spurt produced a wave disturbance with an onset time  $t_0$ . The disturbance traveled about 150 Mm with an average plane-of-the-sky speed of  $\approx 1500 \text{ km s}^{-1}$  (the arrow in Figure 4a), at 07:30:30 arrived at the arcade loop, which gradually expanded above the prominence, and accelerated its lift-off.

With the active role of the prominence, whose eruption presented presumable completion of the flux rope formation, the overlying arcade expanded, being initially driven from inside. Generally, the top part of an arcade is associated with a magnetic separatrix surface, which does not allow plasmas to be transposed inside from outside. The right panels of Figure 3 show that the compression region of swept-up plasmas on top of the expanding arcade evolved. A similar conclusion was drawn by Cheng *et al.* (2011) from the analysis of a different event.

## 2.2. Shock Wave

The initial speed of the disturbance above the active-region core must be equal to the fast-mode speed ( $V_{\text{fast}}$ ), to which the estimated value of  $\approx 1500 \text{ km s}^{-1}$  seems to correspond. When the wave front left the region of high  $V_{\text{fast}}$ , such a high-speed wave must become strongly nonlinear and could rapidly steepen into a shock of a moderate intensity (Afanasyev, Uralov, and Grechnev, 2013). If the shock discontinuity was formed before the passage of the wave through the arcade, then its speed should change abruptly (the blue dashed curves in Figures 4a–4c); otherwise, the kinematical curves should be smoother. As mentioned, we cannot distinguish between the two options from the observations.

On the other hand, all of the measured components of the non-radial eruption reached the speeds of, at least,  $V_{\text{POS}} \approx 700 \text{ km s}^{-1}$  in the field of view of AIA ( $|\mathbf{V}_{\text{max}}| \gtrsim 750 \text{ km s}^{-1}$ ). Such a speed of an ejecta above quiet-Sun regions, where  $V_{\text{fast}}$  is considerably lower, is sufficient to produce a bow shock. The presence of a shock is confirmed by the appearance of a type II burst (Figure 5b). To understand the history of the shock wave, we consider its properties suggested by the type II burst and a propagating ‘EUV wave’.

The dynamic spectrum in Figure 5b was composed from the HiRAS and Learmonth data. For comparison, Figure 5a presents the microwave time profile at 8.8 GHz. The spectrum is complex. It shows a series of type III bursts, of which first three groups correspond to the microwave peaks. Two branches of a type IV emission are present: a quasi-stationary type IV burst around 800 MHz, and a drifting type IV, whose emission was strongest at 400–200 MHz (red). Such drifting type IVs are considered as manifestations of developing CMEs.

A rather strong type II burst, overlapping with an intense series of type IIIs, sharply started at 07:34 and became clearer after 07:37. We invoke the idea of Uralova and Uralov (1994) that a type II emission originates in a coronal streamer, being caused by a shock front compressing its current sheet, thus producing a flare-like process running along the streamer. A particularity of the

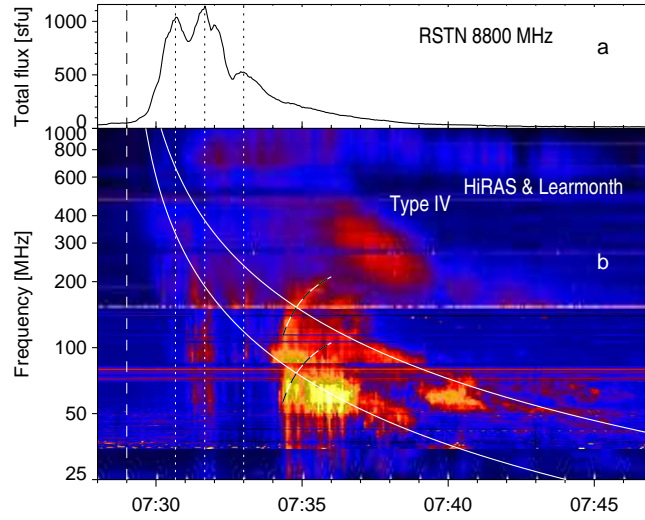


**Figure 5.** The microwave time profile (a) and the dynamic spectrum of the type II burst (b). The white curves outline the calculated trajectory of the type II burst with a wave onset time  $t_0 = 07:29:00 \pm 20$  s marked with the dashed vertical line and a density falloff exponent  $\delta = 2.7$ . The dashed curves outline the reverse-drift portion and its expected fundamental counterpart. The dotted vertical lines mark the microwave peaks to compare them with type III bursts.

burst in Figure 5b is a feature with a reverse drift from 100 to 200 MHz visible during 07:34–07:36 (dashed curve). A parallel dashed curve at 50–100 MHz outlines its possible fundamental-emission counterpart, which is difficult to detect in the figure. The reversely drifting feature looks mirrored relative to the normal drift. Grechnev *et al.* (2011b, 2014a) interpreted such a C-shaped feature as the onset of a type II burst owing to the collision of a quasi-perpendicular shock with a remote streamer. The contact site of the shock front with the streamer bifurcates and moves into opposite directions (Figure 6). While propagating into a higher-density medium, a shock wave strongly dampens. Therefore, such reversely-drifting features are usually marginal. The remarkably long lifetime of the reverse drift here suggests that the shock was rather strong when the type II burst started.

We have outlined the trajectory of the type II burst, using the power-law fit. The pair of the white curves outlines the overall evolution of the drift rate. The estimated wave onset time  $t_0 = 07:29:00$  is shown in Figure 4 with the vertical dotted line; the shaded interval presents the uncertainty of  $\pm 20$  s. This onset time corresponds to the rise phase of the acceleration observed for the most dynamic leading segment of the eruptive filament. Such a situation have been observed in several different events, which we analyzed previously (Grechnev *et al.*, 2011b, 2014b, 2014a, 2013), and supports the impulsive-piston shock excitation scenario. The outermost arcade loop, which we measured (blue in Figure 4b), had a speed of  $< 100 \text{ km s}^{-1}$  at that time; thus, the excitation of a bow shock by the outer surface of the developing CME is excluded. The shock excitation by the flare pressure pulse is unlikely, as shown in Section 2.1.

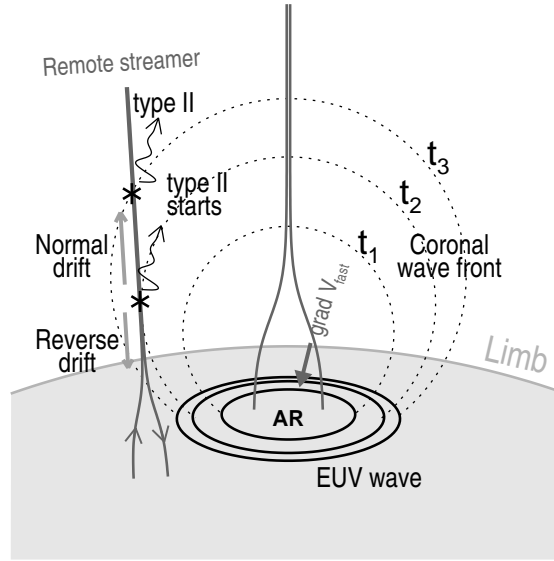


**Figure 6.** Fast MHD shock wave excited by an impulsive eruption in an active region (AR) and a type II burst produced by the shock in a remote streamer. The expanding wave front is represented by the dotted ovals at three consecutive times  $t_1$ ,  $t_2$ , and  $t_3$ , and its near-surface skirt (‘EUV wave’) is represented by the solid ellipses.

These facts can be summarized in the following scenario. The violent filament eruption with an acceleration of up to  $50g_{\odot}$  excited at about 07:29 a substantial MHD disturbance, which initially resembled a blast wave. The wave steepened into a rather strong shock before 07:34:30. This situation corresponds to the impulsive-piston shock excitation scenario (Grechnev *et al.*, 2011b, 2011a; Afanasyev, Uralov, and Grechnev, 2013).

The global propagation of the disturbance is evidenced by the EUVI 195 Å images in Figure 7. The pre-event situation is shown in Figure 7a. The filament eruption occurred in the region denoted with the red frame and produced a disturbance, whose properties are typical of shock-associated ‘EUV waves’. Its propagation was omnidirectional, but not isotropic. The disturbance entered the adjacent coronal hole, CH1, where it ran faster and had a lower brightness. These properties are consistent with its MHD-wave nature. A higher  $V_{\text{fast}}$  in a coronal hole relative to quiet-Sun regions determines i) a faster wave propagation and ii) a lower Mach number, *i.e.*, a weaker plasma compression responsible for the lower brightness (*cf.* Grechnev *et al.*, 2011a). The brightest portion of the ‘EUV wave’ moved initially southwest (Figures 7b and 7c). Then the brightening propagating east became best visible (Figures 7d and 7e). When the front reached the remote AR1167 in Figure 7f, the ‘EUV wave’ apparently bypassed it (this property of ‘EUV waves’, also consistent with a non-uniform  $V_{\text{fast}}$  distribution, as stated by Thompson *et al.* (1999)). No brightening was pronounced northeast of the eruption region; nevertheless, the disturbance propagating in this direction can be followed from the development of two lanes of dimming along AR 11164 in Figures 7c and 7d. Long-lived remote dimming can appear due to the pass of

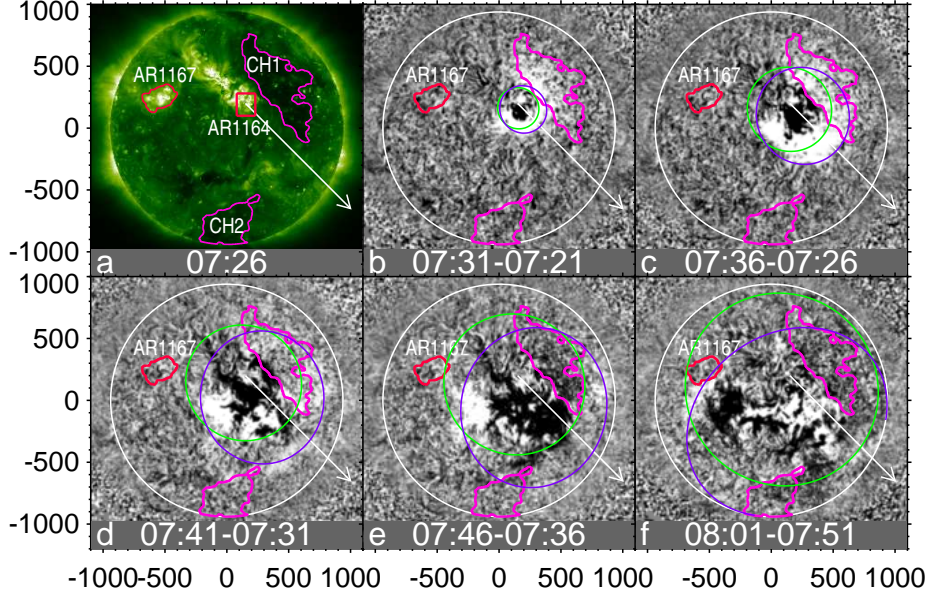


**Figure 7.** STEREO-B/EUVI 195 Å images of Event I. The arrows indicate the direction of the eruption. The contours outline coronal holes (pink) and remote AR1167 (red). (a) Pre-event image. The red frame shows the field of view in Figure 1. CH1 and CH2 are the coronal holes. (b)–(f) ‘EUV wave’ in running-difference image ratios. The green ellipses outline an expected eruption site. The blue ellipses correspond to the moving wave epicenter. The axes show the coordinates in arcsec from the solar disk center.

a shock wave indeed (Grechnev *et al.*, 2013). The running-difference images in the right panel of the 20110224\_euvi\_195\_fulldisk.mpg movie show complex disturbances in a large area southwest from the solar disk center. The disturbances seem to move in different directions, indicating reflection phenomena. This also supports the MHD-wave nature of the ‘EUV wave’.

We tried to outline the global propagation of the ‘EUV wave’ using the power-law approximation,  $r \propto t^{2/(5-\delta)}$  ( $t$  time,  $r$  distance,  $\delta$  formal density falloff exponent) expected for a blast wave, as we did previously. The result of this attempt, with the same wave onset time  $t_0 = 07:29:00$  and  $\delta = 2.0$ , is shown with the green ellipses. Trying to follow the northeastward wave signatures, such as the developing dimming in Figures 7b–7e and the bright east portion of the ‘EUV wave’, we miss its fastest southwest part in Figures 7c and 7d.

To reduce the mismatch, we displace the wave epicenter with a speed of 250–300 km s<sup>−1</sup> following the eruptive filament—the blue ellipses in Figures 7b–7f. They match the southern half of the ‘EUV wave’ front considerably better. However, the green ellipses better reproduce the wave propagation northwest. The estimated surface propagation speed in Figures 7b–7d decrease from  $\approx 900$  to  $\approx 650$  km s<sup>−1</sup> along the arrow, and from  $\approx 560$  to  $\approx 330$  km s<sup>−1</sup> in the opposite direction. All of them exceeded the expected  $V_{\text{fast}}$  above the quiet Sun. Let us see what the revealed properties of the global disturbance mean.



The wave excited at  $\approx 07:29:00$  steepened into the shock before the onset of the type II burst at 07:34:30. This time is between Figures 7b and 7c, in which the ‘EUV wave’ looks similar; probably, the shock appeared still earlier, before the image at 07:31 in Figure 7b. The global disturbance was also observed on the Earth-facing side of the Sun by AIA in the 193 and 211 Å channels (see the movies 20110224\_AIA\_211\_fulldisk.mpg and 20110224\_AIA\_193\_fulldisk.mpg).

Previously we observed a slow progressive displacement of the epicenter of a shock-associated ‘EUV wave’ toward a region of a higher  $V_{\text{fast}}$  (Grechnev *et al.*, 2011b, 2011a, 2013). Such a displacement is due to refraction, being an expected property of MHD waves. However, the wave epicenter displaced in Figure 7 considerably faster and followed the motion of the eruption rather than the  $V_{\text{fast}}$  distribution. While the ellipses with a moving center matched the whole lower skirts of the wave fronts in previous events, here a superposition of the two expanding fronts seems to be present; the green ellipses correspond better to the propagation northeast, and the blue ellipses are closer to the southwest portions. Here, the whole wave front, whose shape was initially close to a spheroid with a nearly radial axis, stretched out afterwards, following the eruption. We have probably met, for the first time, a situation, when the impulsively excited blast-wave-like shock approached the bow-shock regime afterwards (the rear shock propagated freely). A large tilt of the southern wave front portion to the solar surface in Figures 3g and 3h also supports the bow-shock regime.

### 2.3. CME

The eruption has produced a fast CME (the linear-fit speed of  $1186 \text{ km s}^{-1}$  according to the on-line CME catalog (Yashiro *et al.*, 2004; Gopalswamy *et al.*, 2009c; <http://cdaw.gsfc.nasa.gov/CMElist/>)) visible in the LASCO/C2 and C3 images presented in Figure 8. There was an additional complication due to a collision of the fast CME with another, slow CME. The collision is clearly visible in the movies available in the CME catalog.

The slow CME gradually ascended before the collision with a speed of  $\approx 115 \text{ km s}^{-1}$  (from 06:00 to 08:00), presumably from below the streamer belt. The middle of this CME is crossed in Figure 8a, in projection, by a coronal ray, located either in front of the slow CME or behind it. The leading portion of the fast CME appeared in the field of view of LASCO/C2. The dashed arc (same as in Figure 8e) outlines the expected position of the shock front, which we discuss later. The expanding fast CME compressed the slow CME in Figure 8b. In the next images in Figures 8c and 8d, the whole slow CME was deflected.

The collision, which seems to be close to elastic one, has turned the velocity vector of the fast CME. The change of the angle in the LASCO’s plane of the sky is shown by the arrows in Figures 8b and 8f. The shorter arrows correspond to the initial angle of the eruption of  $\approx 25^\circ$  with respect to the east direction. The longer arrows correspond to the final orientation of the fast CME of  $6^\circ$  (*i.e.*, the position angle of  $96^\circ$  listed in the CME catalog).

Figures 8a–8d show the structure of the fast CME. Its leading part appears to consist of the expanding arcade loops. The tangled intertwined structure of a brighter core seems to be the relaxing flux rope formed from the eruptive prominence. No cavity is pronounced.

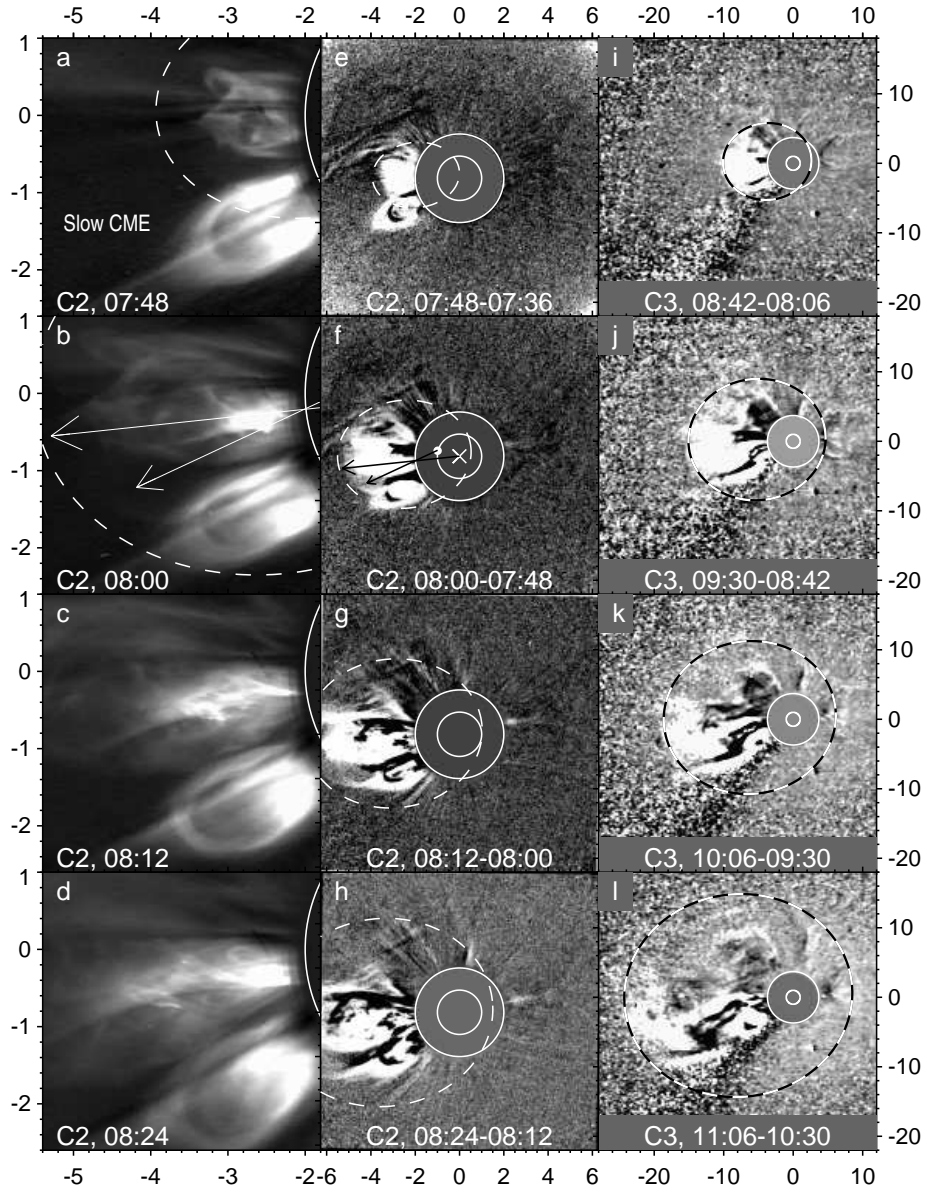


**Figure 8.** The fast coronal transient in the LASCO/C2 (a–d and e–h) and C3 (i–l) images. The structure of the fast CME and its collision with the slow CME visible in C2 images (a–d) with a reduced field of view. The dashed ovals outline the wave signatures in C2 (e–h) and C3 (i–l) images shown with a full field of view as well as in panels (a) and (b). The arrows in panels (b) and (f) indicate the direction of the CME before the collision (shorter arrows) and after it (longer arrows). The slated cross and the small filled circle in panel (f) denote the solar disk center and the eruption center, respectively. The smaller white open circles indicate the location of the solar limb. The larger white open circles denote the inner boundary of the field of view of the coronagraphs. The axes show the coordinates in solar radii from the solar disk center.

The running differences in Figures 8e–8l reveal the traces of the shock wave, mainly from the deflections of the coronal rays. The fast CME in question was preceded by another one, and therefore the outermost disturbances in Figures 8e–8g are irrelevant (the southern part of the transient hints at the relevant traces). We formally fit the kinematics of the leading edge of the transient using the power-law fit with the same wave onset time,  $t_0 = 07:29:00$ , as previously. The density falloff exponent,  $\delta = 2.70$  (corresponding to the mid-latitude Saito model (Saito, 1970; see Grechnev *et al.*, 2011b)), and the reference distance were chosen to achieve a best fit of the leading edge in all of the images in Figure 8.

The ovals outlining the whole shock front in Figure 8 were computed from the fit of the SOHO/LASCO images for the leading edge, and from the fit of the STEREO-B/COR2 images for the lateral expansion. The ovals acceptably match probable shock signatures, but it is difficult to distinguish between the shock front and the trailing CME body in Figures 8i–8l (LASCO/C3). The shock and CME had similar kinematics that corresponds to the bow-shock regime. Eventually, the bow shock produced a glancing blow on STEREO-B spacecraft on 26 February at 08:20, with ICME being pointed by  $\approx 20^\circ$  to the Sun–STEREO-B line, according to our estimate.

#### 2.4. Summary of the Wave History in Event I

A violent prominence eruption above AR 11164 produced a strong omnidirectional wave disturbance propagating with an initial speed of  $\approx 1500 \text{ km s}^{-1}$ . When its front left the region of a high  $V_{\text{fast}}$ , the wave presumably steepened into a shock and started to considerably decelerate in the directions, where it was not followed by the eruption. Its signatures observed in various spectral ranges propagated according to a power-law kinematics expected for a shock wave. All of them had the same onset time, corresponding to the peak acceleration of the prominence. These signatures were i) the trajectory of the type II burst, while its structure was consistent with shock encounters with coronal streamers, ii) the rear part of the ‘EUV wave’, iii) the leading envelope of the white-light CME (which was, most likely, super-Alfvénic). The listed facts confirm that these signatures were different manifestations of a single shock wave, and that the prominence eruption was responsible for its excitation.

Along with an omnidirectional power-law expansion with the same onset time, the wave dome additionally expanded, following the CME. This behavior was dissimilar to the events, which we analyzed previously. This circumstance indicates that in this event, we are probably dealing, for the first time, with a rapid transformation of a leading part of an impulsively excited blast-wave-like shock into a bow shock. Eventually, the shock was detected at the Earth orbit.

### 3. Event II: 11 May 2011

To verify and elaborate the conclusions drawn from the preceding event, which was rather strong, now we consider the weak 11 May 2011 event (GOES importance of B8.1). In this event no HXR emission was detected. It was associated

with the eruption of a filament centered at N25 W54, between small ARs 11207 and 11204. The eruption produced a CME. We analyze the observations of this event carried out by SDO/AIA, SOHO/LASCO, NoRH, and SSRT.

We have produced the NoRH 17 GHz images in steps of 60 s with an integration time of 10 s to enhance the sensitivity. These images had a displaced center enabling us to track the erupting filament as long as possible. The SSRT images at 5.7 GHz covered the main phase of the flare with intervals from 3 to 8 min. The advanced technique used to produce the SSRT images and to calibrate both the SSRT and NoRH images is described by Kochanov *et al.* (2013).

### 3.1. Filament Eruption

Figure 9 presents the initial stage of the eruption observed in the 304 Å channel (characteristic temperature  $5 \times 10^4$  K, top row) and in the 94 Å channel (6.3 MK, bottom row). The rising filament body is dark in 304 Å and blocks radiation from its background indicating its temperature of  $\lesssim 10^4$  K. A similar appearance of the stretching filament threads in 304 and 94 Å suggests a wide temperature range in their brightened parts. Their mutual correspondence indicates the presence of  $\sim 6$  MK plasma. The configuration of the stretched filament threads resembles a flare cusp. The bundles of the threads descending from the cusp are rooted in different ribbons, whose development is shown in the upper row. The lower row presents the development of the flare arcade above the ribbons. The later 94 Å images in Figures 9g and 9h confirm that the hot flare arcade developed at the same place, where the cusp was present. Thus, the flare arcade started to form from the threads belonging to the filament body. The standard-model reconnection between the legs of the pre-flare arcade, which embraced the filament from above, presumably started later on.

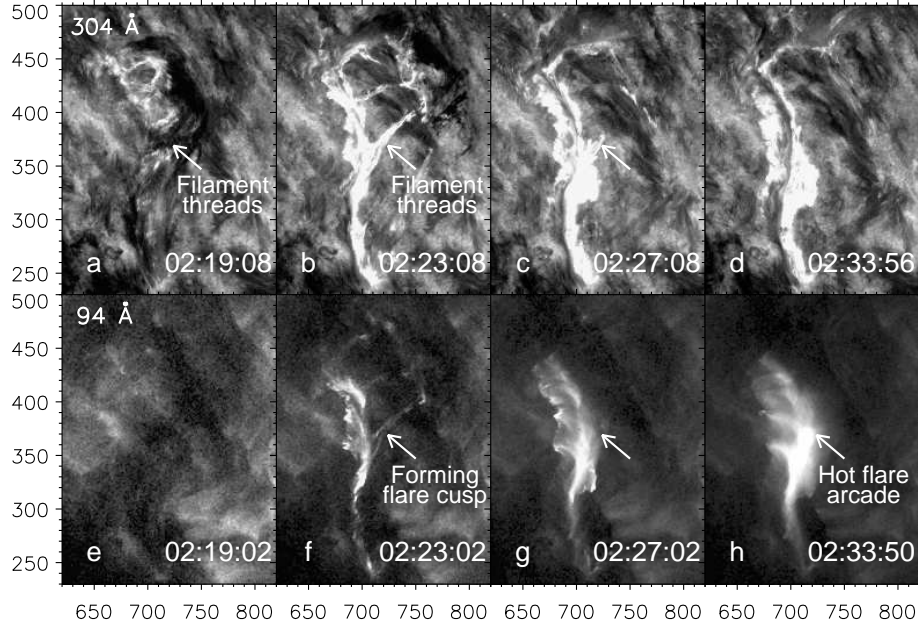
Figure 10 compares the actually observed eruption with the dual-filament CME initiation model (Section 1.1; Uralov *et al.*, 2002). Figure 10a shows the filament in 304 Å (similar to Figure 9b). A running-difference 193 Å image in Figure 10b reveals two filament segments, a slower thicker north one and a faster thinner south one. The heated south threads discussed above seem to be shared by both segments. A striking similarity between the observations and model supports the formation of the flare cusp from the filament threads. The model predicts strengthening the propelling force, when two segments combine.

### 3.2. Expansion of the Filament and the Overlying Arcade

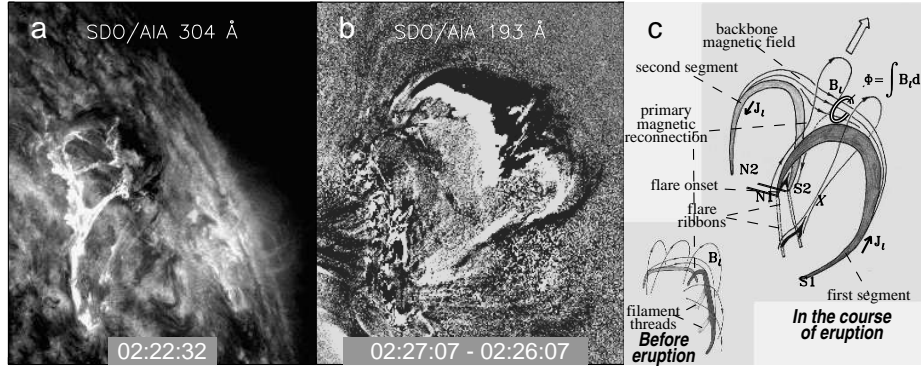
The expansion of the eruptive structures is presented in Figure 11. The eruptive filament is clearly visible in 304 Å and somewhat poorer in 193 Å. The thick north filament segment looks very similar in the 17 GHz and 304 Å images. We measured from these images the kinematics of the expanding filament's top in the direction between the two segments with an uncertainty  $< 8$  Mm. We also made the measurements of a poorer accuracy from the 17 GHz images, whose field of view reaches  $1.5R_{\odot}$  (422 Mm from the eruption site), until 02:43:05.

Figure 12 shows the kinematic plots of the measured filament's part and a faint oval above it associated with the top of a pre-eruption arcade, as discussed





**Figure 9.** Filament eruption on 11 May 2011 observed by SDO/AIA in 304 Å (top row) and in 94 Å (bottom row). The positions of all the arrows are the same.



**Figure 10.** The 11 May 2011 event. Comparison of the eruptive filament observed with SDO/AIA in the 304 Å channel (a) and a later running-difference 193 Å image (b) with the dual-filament model (c; adapted from Uralov *et al.* (2002)).

below. The solid curves present the fit. Initially, the filament gradually rose with a speed of  $\approx 21 \text{ km s}^{-1}$ , which is typical of the initiation stage. The filament underwent an acceleration of  $0.5 \text{ km s}^{-2}$  around 02:17:00, and sharply ( $\approx 3.3 \text{ km s}^{-2}$ ) accelerated again at  $02:22:05 \pm 5 \text{ s}$  to a final velocity of  $V_{\text{max}} \approx 320 \text{ s}^{-1}$ , which did not change after 02:25. The spine of the coupled filament segments expanded slightly faster than the clearly visible measured feature, with a velocity of  $340 \text{ s}^{-1}$ , which we use in further measurements.

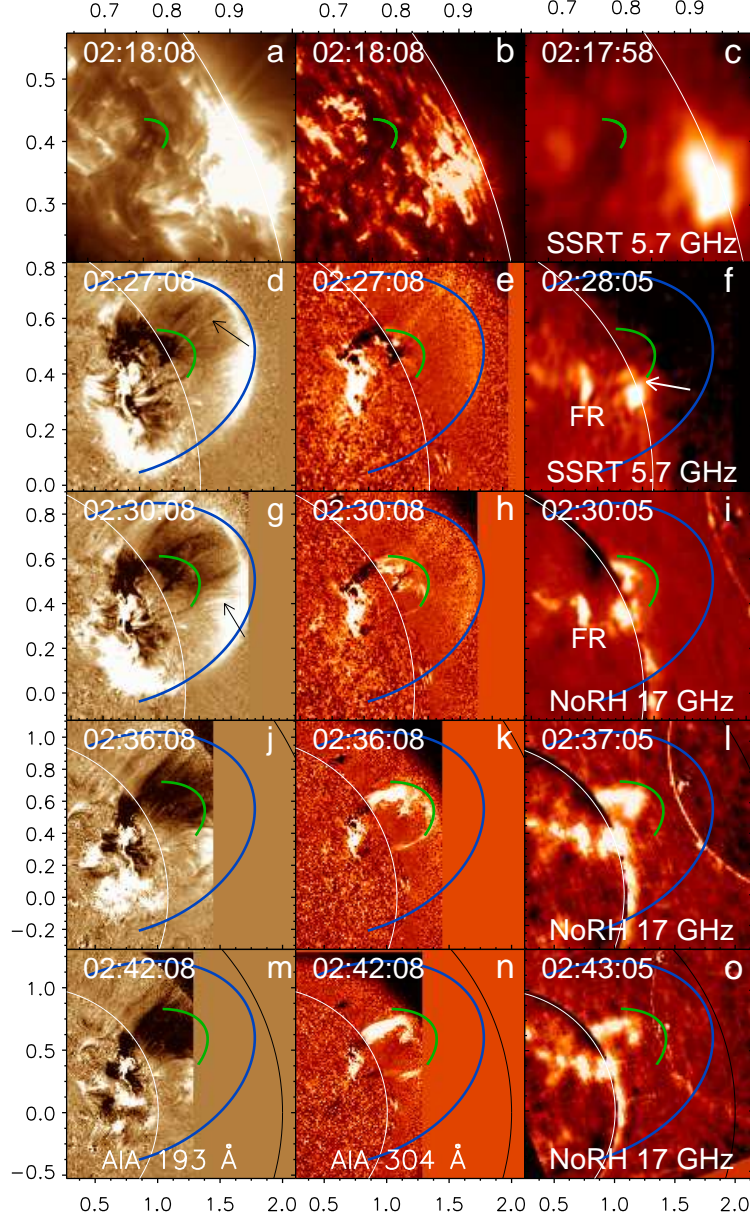


**Figure 11.** Expansion of the erupting filament and the arcade above it in SDO/AIA 193 and 304 Å as well as microwave images: SSRT at 5.7 GHz (c,f) and NoRH at 17 GHz (j,i,o). The AIA images in the second to bottom rows are the ratios to the images observed in the corresponding channels at 02:18:08. All of them were rotated to 02:27:00. The quiet-Sun’s disk was subtracted from the microwave images. The flare region is labeled ‘FR’ in panels (f) and (i). All the images are resized according to the measured kinematics in Figure 12 to keep the visible size of the expanding eruption fixed. The blue arc outlines the arcade. The green arc outlines the filament. The white arc outlines the solar limb. The black arc in two lower rows corresponds to the inner boundary of the LASCO/C2 field of view of  $2R_{\odot}$ . The axes show the coordinates in solar radii from the solar disk center.



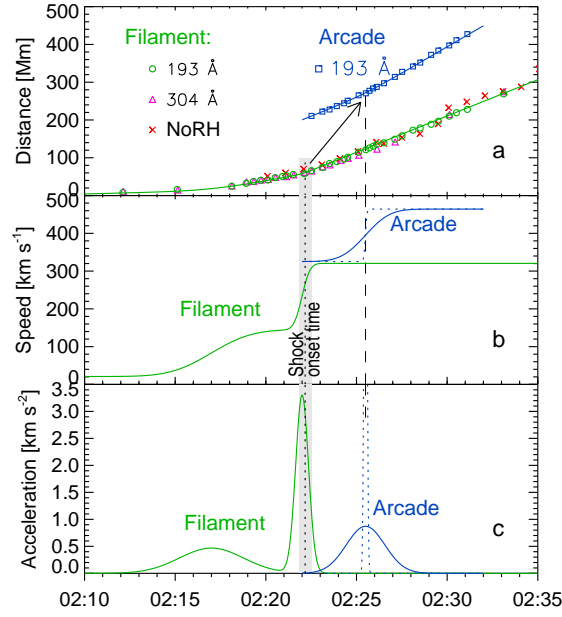


**Figure 12.** Measurements of the kinematics for the eruptive filament and arcade in Event II from the SDO/AIA images in 304 and 193 Å and the NoRH 17 GHz images. The symbols show the initial straightforward measurements. The solid curves present the fit. The thin dashed lines correspond to a possible shorter acceleration of the arcade. The dotted vertical line denotes the estimated shock onset time, and the shaded interval presents its uncertainty. The dashed vertical line corresponds to the acceleration peak time of the arcade. The arrow in panel (a) indicates a disturbance propagating from the erupting filament to the arcade.

The expansion of the arcade was measured in a nearly the same direction as that of the filament. Initially, the oval on top of the arcade was not sharp, and the uncertainties were larger, about 15 Mm. According to the fit in Figure 12, the arcade expansion accelerated from  $325 \pm 5 \text{ km s}^{-1}$  to  $465 \pm 5 \text{ km s}^{-1}$ . The observations allow us to estimate only the upper limit for the duration of the acceleration and the lower limit for its maximum of  $\gtrsim 0.9 \text{ km s}^{-2}$ . Similarly to the situation in Event I, the use of a considerably stronger acceleration does not result in a pronounced difference in the outline of the arcade in the images. The center time of the acceleration is certain,  $02:25:30 \pm 10 \text{ s}$ .

The sequence of phenomena presented in Figure 12 is similar to Event I (*cf.* Figure 4). The eruptive filament in Event II underwent a strongest acceleration around 02:22:05 and produced a wave disturbance with an onset time  $t_0 = 02:22:10 \pm 20 \text{ s}$  (the vertical dotted line). The disturbance indicated by the arrow in Figure 12a traveled about 200 Mm with an average plane-of-the-sky speed of  $\approx 1000 \text{ km s}^{-1}$ , reached at 02:25:30 the arcade (the vertical dashed line), which gradually expanded above the filament, and impulsively accelerated its lift-off.

Figure 11 shows the expansion of the eruptive filament and the arcade above it as observed by SDO/AIA in 193 Å (left column), in 304 Å (middle column), and in microwaves by SSRT and NoRH (right column). All of the images are

progressively resized according to the measured kinematics, to keep the size of the eruption unchanged. The top of the expanding filament and the arcade are outlined with the oval arcs, whose radii were calculated from the corresponding fit in Figure 12 with a mentioned correction.

Microwave images in the right column show the erupting filament from its initial position up to large distances. The dark filament is visible in the SSRT images at 5.7 GHz with a higher contrast against the solar disk, whose brightness temperature is  $T_{\text{QS}(5.7)} = 16000$  K, than in the NoRH images with  $T_{\text{QS}(17)} = 10000$  K. The thin south filament segment is detectable in the 5.7 GHz image in Figure 11f due to the overlap with a bright region on the limb. Then we use the higher-sensitivity NoRH images at 17 GHz, where the bright filament is better visible against the sky, than in the SSRT ones. The thick north filament segment appears similar in the 17 GHz and 304 Å images. The measured kinematics of the eruptive filament shows a good correspondence with all the images. Both filament segments in 304 Å were joined by an oval spine corresponding to the backbone field in the dual-filament model in Figure 10c.

The faint bright oval in Figure 11d and 11g is similar to the arcade top in Event I. Here, the orientation of the flux rope’s axis indicated by the filament and flare ribbons was close to the plane of the sky. Thus, the oval surrounding the eruptive filament cannot be the cross section of a flux rope. On the other hand, nearly radial bright thin structures faintly visible inside the oval (*e.g.*, those indicated by the arrows in Figures 11d and 11g) resemble the outer arcade loops, whose planes had small angles with the line of sight. This identification corresponds to the orientation of the filament and ribbons. A separatrix surface should exist above the arcade. Thus, the arcade top prevented any plasma motions from outside into its interior. Its expansion resulted in the appearance of a compression region constituted by the swept-up plasmas on its top.

The expansion of the arcade ‘membrane’ results in a rarefaction in the volume enclosed by the arcade. As the 193 Å ratio images in the left column show, dimming behind the expanding arcade developed. The observations shed light on its cause. The brightness  $B$  in EUV images is proportional to the column emission measure. The brightness in the center of an expanding volume of a linear size  $L$  with a fixed total number of emitting particles should be  $B \propto EM/A \propto n^2 L = (N_0/V)^2 L \propto 1/L^5$ . The expansion alone results in this dramatic brightness decrease. The resulting density depletion should cause a siphon effect to fill the dimmed volume by plasma flowing from below. This circumstance is consistent with plasma flows from dimmings revealed by Harra and Sterling (2001). This phenomenon seems to be a secondary effect of the expansion due to the CME lift-off and is expected to be commonly present.

The same factor of  $B \propto 1/L^5$  applies to the microwave brightness. For this reason, eruptions observed in EUV and microwaves rapidly fade away. Note that the Thomson-scattered light responsible for the white-light transients is controlled by a much softer factor of  $B \propto 1/L^2$ , which grants the opportunities to observe CMEs up to very large distances from the Sun.

As mentioned, the arcade accelerated at 02:25:30  $\pm 10$  s to a final speed of  $465 \pm 5$  km s<sup>-1</sup> with a measured acceleration of  $\gtrsim 0.9$  km s<sup>-2</sup>. Its actual duration could be less, and the maximum value could be higher. In any case,

the acceleration of the arcade lagged behind that the prominence, as in Event I. The temporal relation between the observed phenomena in Figure 12 and the estimated velocities of the erupting filament, arcade, and wave demonstrate that the wave drove the arcade, but not *vice versa*. The prominence was more dynamic, which indicates that it was the major driver of the whole eruptive event. The fast prominence eruption with an acceleration up to  $3.3 \text{ km s}^{-2}$  ( $\approx 12g_{\odot}$ ) could produce a shock wave.

### 3.3. Shock Wave

There are manifestations of a shock wave excited in this event indeed. Figure 13g shows a dynamic spectrum composed from the records made with the Learmonth, Culgoora, and the STEREO-A/WAVES *Radio and Plasma Wave Investigation* (Bougeret *et al.*, 2008) spectrographs. At 02:27:30, a type II burst suddenly started. It had a few pairs of bands, of which three are outlined with the curves of different line styles. Two pairs of the bands began nearly simultaneously and resembled band-splitting, which is usually related to the emissions from electrons accelerated in the upstream and downstream regions of the shock (Smerd, Sheridan, and Stewart, 1974). However, the distance between the bands belonging to different pairs was large. The traditional interpretation accounts for two pairs of bands only. Alternatively, Grechnev *et al.* (2011b) proposed an explanation of a large band-splitting by a passage of the shock front over remote streamers located close to each other (the geometry similar to that shown in Figure 6). This process can account for a more complex multi-band structure of a type II burst. Figure 13f and the movies 20110511\_AIA\_193\_eruption.mpg and 20110511\_AIA\_193\_spectrum.mpg really show two small ray-like structures located aside of the eruption. They were inflected by a disturbance propagating from the erupting structure. The contours calculated for a single decelerating blast wave match the evolution of the drift rate for all bands of the type II burst. We have estimated the shock onset time  $t_0 = 02:22:10 \pm 20 \text{ s}$ , which corresponds to the strongest acceleration of the erupting filament and to various shock manifestations.

The calculated propagation of the shock front is shown in Figure 13 and movie 20110511\_AIA\_193\_spectrum.mpg in comparison with the dynamic spectrum. The panels of each row present the same AIA 193 Å image processed in different ways. The images in the left column are fixed-base ratios, which show the erupting filament better. The images in the right column are running-difference ratios, which allow one to see the expanding arcade and an ‘EUV wave’ developing at its base. The ovals represent the calculated portions of the wave fronts with  $t_0 = 02:22:10$  and  $\delta = 2.7$ . Here we do not analyze the near-surface propagation of the shock wave, and therefore the ovals are not closed. The three pairs of images present different times: shortly after the wave onset (Figures 13a and 13b), during the passage of the wave through the arcade (Figures 13c and 13d), and at the onset of the type II burst (Figures 13e and 13f). These times are marked on the dynamic radio spectrum in Figure 13g with vertical lines, whose styles and colors correspond to the ovals. The arrows in the third row indicate the inflected small streamers, in which the sources of the type II burst could be

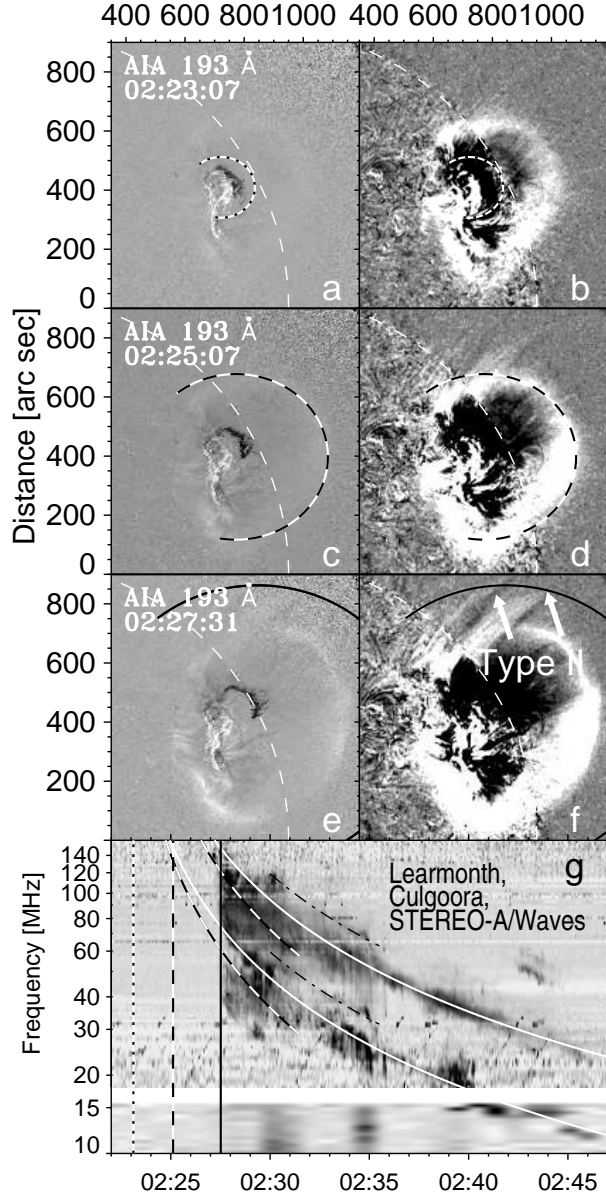


**Figure 13.** Expanding wave front in the SDO/AIA 193 Å images in comparison with a type II burst. The left column shows fixed-base ratios at 193 Å to reveal the eruptive filament. The right column shows running-difference ratios in 193 Å to reveal the expanding arcade and deflected small streamers north to it. The thick ovals present the calculated wave fronts with  $t_0 = 02:22:10$ ,  $\delta = 2.7$ . The thin dashed arc denotes the solar limb. (g) Dynamic spectrum of the type II burst. Three pairs of the curves with the same shock onset time,  $t_0$ , outline different harmonic pairs of the bands presumably emitted from different streamers hit by the same shock front. The vertical lines mark the times of the images above. The colors and line styles of the ovals correspond to those of the vertical markers on the spectrum.

located. The estimates of the distances and velocities from dynamic spectra are uncertain by an unknown density multiplier; the points in question are the wave onset time and the trajectory of the type II burst.

Figure 13 confirms that the sharply erupting filament excited a shock wave, which passed through the arcade, accelerated its expansion, and then reached two small remote streamers, thus causing the generation of the type II burst in them. Two additional facts support the presence of a shock wave. i) A slower surface trail (‘EUV wave’) of the expanding bright oval in the right column corresponds to the idea of Uchida (1968), initially proposed for Moreton waves. ii) The 20110511.AIA\_193\_eruption.mpg movie shows that the southeast portion of the ‘EUV wave’ is reflected from a coronal hole at about 02:48, and a backward-reflected front runs slower than the incident front (*cf.* Gopalswamy *et al.*, 2009a) that is expected for a shock wave (Grechnev *et al.*, 2011b). These facts confirm the MHD shock-wave nature of the propagating ‘EUV wave’.

We have applied a power-law fit with the same parameters as in Figure 13 to the LASCO observations in Figure 14. To see the expanding features better and facilitate their comparison with each other, all of the images are progressively resized to keep the size of the expanding wave front unchanged. The ovals represent the calculated fronts of the shock wave, which decelerated from the initial velocity of  $> 1200 \text{ km s}^{-1}$  to  $\approx 550 \text{ km s}^{-1}$  in the latest images, becoming comparable to the solar wind speed. The wave is manifested at large distances in the deflections of coronal rays indicated by the arrows in the upper row (*cf.* Sheeley, Hakala, and Wang, 2000; Vourlidas *et al.*, 2003; Gopalswamy *et al.*, 2009b). The ovals encompass the outer boundary of the CME toward the regions above the north pole and match the wave traces ahead of the CME up to  $17R_{\odot}$ . The shock wave in this event eventually decayed into a weak disturbance.

### 3.4. CME

The resizing representation can help to find the nature of the components of the CME produced in this event. Figure 15 presents fixed-base image ratios to compare the expanding arcade in Figure 15a and the coupled filament in Figure 15b with the CME structure in Figures 15c–15f. The ovals outlining the arcade (blue) and filament (green) help in identifying the CME components with their progenitors. The expansion speed used to resize the images and to plot the ovals was constant,  $340 \text{ km s}^{-1}$  for the filament and  $465 \text{ km s}^{-1}$  for the arcade.

The ovals outlining the filament and the arcade match the CME core and frontal structure (FS) in earlier LASCO images, respectively. The frontal structure consisted of nearly radial loops, whose planes had acute angles with the line of sight. These facts confirm our identification of the bright oval in Figure 15a with an arcade, and show that the arcade was a progenitor of the frontal structure. The core originated from the eruptive filament, as commonly recognized. The features leading the frontal structure, like the distorted streamers indicated by the arrows, reveal the wave ahead of the CME.

The core lags behind the dashed outline in later images, Figures 15c–15f. The filament, which initially drove the expansion of the arcade, relaxed and decelerated. The arcade became the inertial frontal structure. The impulsive-piston-driven shock ran well ahead of the CME, like a decelerating blast wave.



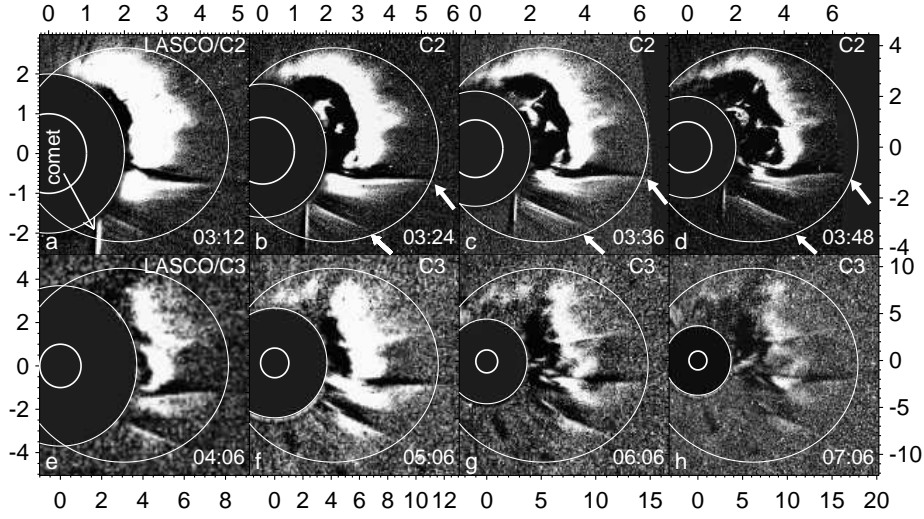


**Figure 14.** Traces of the expanding wave front in running-difference ratios produced from LASCO/C2 images (top row) and C3 ones (bottom row). The ovals represent the calculated wave fronts. All the images are resized to keep the visible size of the expanding wave front fixed. The axes show the coordinates in solar radii from the solar disk center. The white solid circles denote the solar limb and the inner boundaries of the LASCO/C2 and C3 field of view.

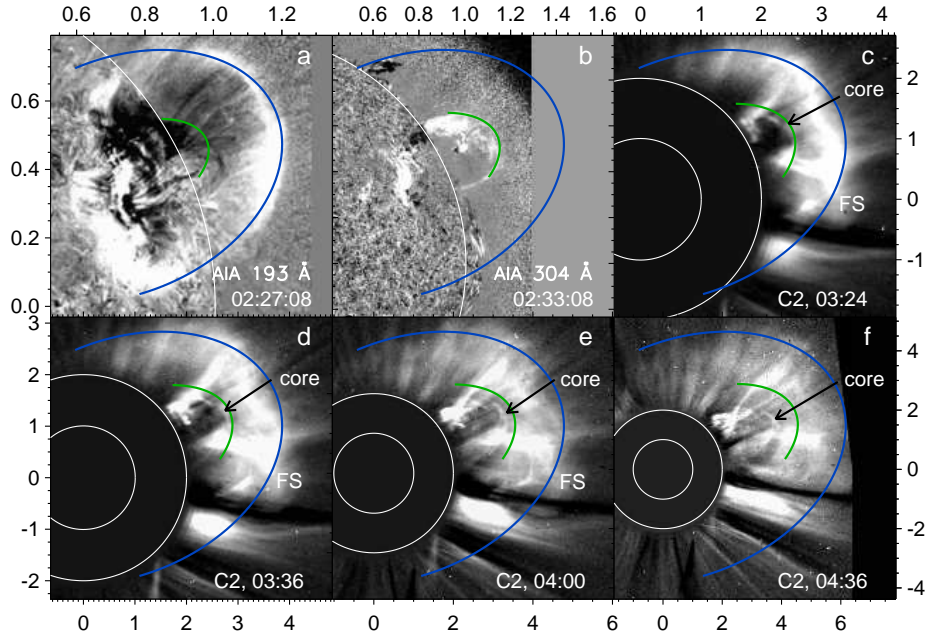


**Figure 15.** CME observed by LASCO/C2 in the 11 May 2011 event (c–f) in comparison with the arcade (a, AIA 193 Å) and erupting filament (b, AIA 304 Å). All of the images are resized to keep the size of the CME fixed. The ovals outline the expanding frontal structure FS (blue) and core (green) according to the measured speeds of the arcade and filament, respectively. The axes show the distances from the solar disk center in solar radii. The white solid circles denote the solar limb and the inner boundary of the LASCO/C2 field of view.



### 3.5. Summary of the Wave History in Event II

Although Event II (B8.1) was considerably weaker than Event I (M3.5), the observations reveal the same wave excitation scenario in both events. Here, the erupting filament produced a wave disturbance with an onset time  $t_0 = 02:22:10$ . The propagating wave reached the arcade, which gradually expanded above the filament, and accelerated its lift-off. Then the wave deflected two remote streamers. The wave propagation visible in EUV, as well as its farther signatures in white-light LASCO images, follow a single power-law distance-time plot expected for a shock wave, with the same  $t_0$ . The trajectory of the type II burst also corresponds to a power-law shock-wave kinematics with the same  $t_0$ , and its structure corresponds to the shock encounter with the mentioned streamers. Thus, all of these signatures were different manifestations of a single shock front, which originated in the filament eruption.

In Event II, the CME body was slow ( $465 \text{ km s}^{-1}$ , as we showed), and the shock wave eventually decayed into a weak disturbance. The different speeds of the CME bodies determined the different wave evolutions in the two events, although their origins were similar.

## 4. Discussion

The chain of phenomena observed in Events I and II suggest the following scenario. The activation of a filament in the initiation phase precedes the flare, being probably related to heating in the filament or/and its coronal environment. These processes, which respond in a gradual rise of the SXR emission (Event I), commence the final formation of an eruptive flux rope. The initial rise of the filament stretches magnetic threads passing through its body and ending at the solar surface, so that they cross each other and form a cusp-like configuration (Events I and II) above the future flare site. The cusp is constituted by quasi-antiparallel magnetic fields, which start to reconnect. This results in heating in this region (Event II). A violent MHD instability (probably, the torus one, Event I) develops, increasing the acceleration of the filament. The flare develops, being slightly delayed after the filament acceleration (Event I). The sharply accelerating filament i) forces the magnetic structures above it to expand, and ii) produces a substantial MHD disturbance, which rapidly steepens into a blast-wave-like shock. Then the acceleration of the filament ceases, its magnetic structure relaxes, and its combination with the structures expanding above it constitute a CME. Eventually, the shock ahead of the CME either changes to the bow-shock regime, if the CME is fast (Event I), or decays otherwise (Event II). Its flanks and rear propagate freely. This picture of a flare-related eruption seems to be different from non-active-region eruptions of quiescent filaments.

### 4.1. Formation of a Flux Rope and Flare Initiation

A low-lying progenitor of a flux rope often shows up as a pre-eruption filament (prominence). It is frequently considered as a passive part of a larger flux rope,

whose expansion creates a CME. By contrast, a pre-eruption filament in an AR carries large electric currents, as the linear force-free approach ( $\alpha = \text{const}$ ) confirms. The density of the electric current is proportional to the magnetic field strength, being typically larger near the solar surface. The development of an MHD current-driven instability (kink or torus) is only possible, if the distribution of the  $\alpha$  parameter is inhomogeneous. Even in the situation of the non-linear force-free magnetic field, the major current-carrying part of a flux rope is expected in its bottom part, *i.e.*, in a low-lying structure like a pre-eruption filament, where  $|\alpha|$  is maximum. Thus, a filament (or its analog) in an active region appears to be the major progenitor of the eruptive flux rope, whose instability increment is governed by stronger, lower, smaller-scale magnetic fields, while the influence of the weaker, larger-scale environment is less important.

The magnetic field and plasma continuously occupy the whole magnetic environment of an AR. They are topologically bounded by the separatrix surface, which confines the coronal cavity surrounding a prominence, and probably develops later into the frontal structure of a CME. The cavity is similar to a magnetic ‘cocoon’ enveloping the pre-eruptive filament and consisting of sheared current-carrying loops, which are rooted in the photosphere. The cavity is traditionally identified with a ‘perfect’ magnetic flux rope, which is only rooted in the photosphere by two ends, being disconnected elsewhere.

A real pre-eruption filament has numerous lateral connections to the photosphere with its threads (barbs) on both sides of the magnetic neutral line. The perfect flux rope not yet exists; its progenitor is the magnetic structure of the filament inside the magnetic cocoon. Their combination is the initial structure in the CSHKP model, in which magnetic loops of the expanding cocoon stretch out, reconnect under the eruptive filament, and form the expanding flux rope. The eruptive filament is located inside the cocoon; its external boundary is the separatrix surface. The joint expansion of all of these structures is observed as a CME.

In our consideration, the formation of the perfect flux rope is necessary to trigger the main stage of the ‘standard’ flare. The flux rope starts to form from breaking its lateral connections to the photosphere leading to the formation of primary flare ribbons by reconnection between the filament threads crossing each other, rather than CSHKP-reconnection of magnetic field lines, which initially were not shared by the filament. The opposite-polarity magnetic field of the filament threads, which participate in the primary reconnection, pass through the body of the filament and embrace it, being its intrinsic components. The primary reconnection is not a simple reconnection of a single pair of flux tubes, as in the tether cutting model. Instead, this is a wavelike series of reconnection events between the threads, running along the filament and the polarity inversion line.

In non-active-region eruptions of quiescent filaments, which are easier to observe, the increments of an instability (*e.g.*, a torus one) corresponding to the filament and cocoon should not be much different from each other. The filament and the larger cocoon expand jointly as a single, self-similar CME structure practically from the very start. The radial profile of the plasma velocity inside the CME is linear relative to the expansion center. These circumstances produce an impression of a passive role of the filament in the eruptive process.



on top of the CME bubble makes its boundary visible. The compressed oval layers might be a rather common phenomenon, disclosing developing CMEs (see, *e.g.*, Cheng *et al.*, 2011). Such bright ovals could occasionally be observed by SOHO/EIT as sharp ‘S-waves’, although the probability to catch them with EIT was low (7% according to Biesecker *et al.*, 2002) due to its insufficient imaging rate. As an ‘S-wave’ can actually be the compressed plasma layer swept-up by a gradually expanding arcade, relating ‘S-waves’ to shock waves (*e.g.*, Ma *et al.*, 2011) might be not correct. The brightenings associated with the near-surface parts of the separatrix surfaces, or ‘quasi-stationary EIT waves’, appear to represent the ‘field-stretching’ effects (Chen, Fang, and Shibata, 2005). An example is a brightening south from the eruption site in Event II, around  $[750'', 80'']$  from the solar disk center. It is visible in the left panel of the 20110511\_AIA\_193\_eruption.mpg movie.

The traveling ‘EUVI waves’ in Events I and II were, most likely, near-surface skirts of the expanding domes of MHD shock waves, in agreement with Uchida (1968) and Thompson *et al.* (1999). Their MHD-wave nature is confirmed by their velocities, reflection phenomena, and accordance of their propagation up to very large distances (more than the solar hemisphere in Event I) with the fast-mode speed distribution. These facts is difficult to reconcile with non-wave interpretations, such as the mentioned field-stretching model of Chen, Fang, and Shibata (2005) or the interchange-reconnection model of Attrill *et al.* (2007). While alternative interpretations of ‘EUV waves’ (see, *e.g.*, Wills-Davey and Attrill, 2009; Gallagher and Long, 2011 for a review) are mostly focused on near-surface phenomena, we established in Events I and II the kinematic correspondence between them, the trajectories and structures of type II bursts, and the CME expansion.

The shock front ahead of the CME gains energy from the trailing ‘piston’, which spends it to sweep up plasmas. Thus, the shock front kinematically resembles a self-similar blast wave propagating in plasma with a density falloff  $\delta \approx 2.7$ , close to the Saito model. For the shock propagation along the solar surface,  $\delta = 0$  might be expected, but this is not the case due to the radial inhomogeneity of the solar corona (see Grechnev *et al.*, 2008, Section 4.5). The kinematics of the shock front, which is not followed by a separatrix surface laterally, can formally be described with  $\delta > 0$ . The results of this approach are close to the modeled shock propagation (Afanasyev and Uralov, 2011; Grechnev *et al.*, 2011a).

The rapidly decelerating near-surface portion of the wave front can be observed in the  $H\alpha$  line as a fast Moreton wave, usually not far from the eruption site, and as a slower ‘EIT wave’ in EUV at larger distances. Having encountered a coronal streamer, the shock front compresses its current sheet causing magnetic reconnection there. The cumulation effect intensifies the flare-like process running along the streamer. A type II burst appears (see Figure 6).

The bow shock continuously driven by the outer surface of a super-Alfvénic CME (see, *e.g.*, Vršnak and Cliver, 2008; Reames, 2009) can be actualized in the case of a supersonic plasma flow around the outer surface of the CME bubble. Two conditions are important for this regime: i) the existence of a stagnation point in the plasma flow on the surface of the body, and ii) the velocity of the stagnation point must exceed the ambient  $V_{\text{fast}}$ . Such a plasma flow does not yet exist at the early CME formation stage. In the bow-shock regime, the CME size

and speed ( $V_{\text{CME}} > V_{\text{fast}}$ ) determine the position and intensity of the stationary shock ahead of the CME. The bow-shock problem does not consider the kinematical differences of the structural CME components preceding the appearance of the shock, including the large difference of their accelerations from the self-similar regime. With strong accelerations measured for the impulsively erupting filaments in Events I and II, the impulsive-piston mechanism excited shock waves effectively and rapidly. The kinematics of the whole CME determines whether or not the frontal portion of the wave transforms into the bow shock afterwards.

The CME frontal structure in Event II had a nearly constant speed of  $465 \text{ km s}^{-1}$  up to  $7R_{\odot}$ , unlikely exceeding the Alfvén speed (see, *e.g.*, Mann *et al.*, 2003). The shock wave quasi-freely propagated well ahead of the CME, being detectable up to  $17R_{\odot}$  in Figure 14, where it decelerated to  $\approx 530 \text{ km s}^{-1}$ , comparable to the solar wind speed. This shock wave eventually decayed into a weak disturbance. By contrast, the blast-wave-like shock impulsively excited in Event I later showed indications of its approach to the bow-shock regime, even when propagating over the solar surface. The transition into a bow shock at large distances from the Sun was anticipated by Grechnev *et al.* (2011b, 2013). The early appearance of the bow shock in Event I was favored by the conspicuously non-radial motion of the eruption and its high speed, which was rapidly reached at a small height. As a result, the rapidly moving southwest part of the ‘EUV wave’ in later EUVI images of this event probably was a near-surface trail of a bow shock.

The deceleration of coronal transients can be due to different forces. They are the gravity and magnetic tension of structures, which remain anchored on the Sun. The plasma extrusion by the expanding CME and the aerodynamic drag from the solar wind flowing around the CME (*e.g.*, Chen, 1996; Vršnak and Gopalswamy, 2002) also spend its energy. We cannot distinguish which retarding force dominated at each stage and to detect the transition from one deceleration regime to another. Presumably, the CME core decelerated in Event II (Figures 15d–15f) mainly due to the magnetic tension; deceleration due to the plasma extrusion dominated during the initial extra-radial expansion of the CMEs; and the aerodynamic drag was significant in the bow-shock regime.

One more consequence of the plasma extrusion by expanding CMEs is the development of dimming. The brightness in EUV and SXR images is proportional to the column emission measure, *i.e.*, the squared density. The CME expansion alone results in a dramatic rarefaction of the involved volume observed as dimming. A strong pressure gradient appears and causes a secondary plasma outflow in the footprint regions of a CME (Harra and Sterling, 2001). The utmost velocity of the outflow is limited by the sound speed (Jin *et al.*, 2009).

## 5. Summary

The observations considered in Sections 2 and 3 appear to confirm the scenario of Hirayama (1974) incorporated into the CSHKP model with further elaborations mentioned in Section 1. The results update the model and specify the flare–CME relations, as well as the excitation and evolution of associated shock waves.

The observations indicate that the flare arcade starts to form from the threads of the filament body. This implies involvement in the eruptive-flare reconnection

processes of considerably lesser-height, *i.e.*, stronger magnetic fields with higher gradients. This can help to understand some observational challenges.

The flux ropes were found by Qiu *et al.* (2007) to be mainly formed via reconnection process, and independent of pre-existing filaments, whose role was unclear. Our results indicate that flux ropes form in the same way from their filament-like progenitors, while the possibility to observe a filament depends on its predominant temperature and density and, possibly, other conditions.

All observational facts considered here confirm that we dealt with fast MHD shock waves, initially excited in the low corona by sharply erupting flux ropes, and neither by a flare pressure pulse nor by the outer surface of a CME. The initial impulsive-piston shock excitation during the early flare rise was responsible, with minor variations, for the shocks observed in a number of different events, ranging from the GOES B class up to the X class (Meshalkina *et al.*, 2009; Grechnev *et al.*, 2011b, 2014a, 2013). The concept, which related the source of a type II emission to the current sheet of a coronal streamer stressed by a shock front, has accounted for the structural features of the observed type II bursts. The evolution of shock waves and their manifestations in EUV and white-light images, and dynamic radio spectra, have been quantitatively reconciled with each other. They get further confirmation from a recent study of Kwon *et al.* (2013).

**Acknowledgements** We appreciate the efforts of the colleagues operating SSRT and NoRH. We thank G. Rudenko, S. Anfinogentov, K.-L. Klein, K. Shibasaki, L. Kashapova, N. Meshalkina, and Y. Kubo for their assistance and discussions, and anonymous reviewers for useful remarks. Our special thanks to reviewer 2 for the valuable recommendations, which significantly helped us to bring the paper to its final form. We are grateful to the instrumental teams operating SDO/AIA, STEREO/SECCHI, Wind/WAVES and S/WAVES, RHESSI, SOHO/LASCO (ESA & NASA), NICT, Culgoora Radio Spectrograph, USAF RSTN network, and GOES satellites for the data used here. We thank the team maintaining the CME Catalog at the CDAW Data Center by NASA and the Catholic University of America in cooperation with the Naval Research Laboratory. This study was supported by the Russian Foundation of Basic Research under grants 11-02-00757, 12-02-00037, 12-02-33110-mol-a-ved, 12-02-31746-mol-a, and 14-02-00367; the Integration Project of RAS SD No. 4; the Program of basic research of the RAS Presidium No. 22, and the Russian Ministry of Education and Science under projects 8407 and 14.518.11.7047.

## References

- Afanasyev, A.N., Uralov, A.M.: 2011, *Solar Phys.* **273**, 479. DOI: 10.1007/s11207-011-9730-9
- Afanasyev, A.N., Uralov, A.M., Grechnev, V.V.: 2013, *Astron. Rep.*, **57**, 594. DOI: 10.1134/S1063772913080015
- Alissandrakis, C.E., Kochanov, A.A., Patsourakos, S., Altynsev, A.T., Lesovoi, S.V., Lesovoya, N.N.: 2013, *Publ. Astron. Soc. Japan* **65**, SP1, S8. DOI: 10.1093/pasj/65.sp1.S8
- Antiochos, S.K., DeVore, C.R., Klimchuk, J.A.: 1999, *Astrophys. J.* **510**, 485. DOI: 10.1086/306563
- Attrill, G.D.R., Harra, L.K., van Driel-Gesztelyi, L., Démoulin, P.: 2007, *Astrophys. J. Lett.* **656**, L101. DOI: 10.1086/512854
- van Ballegoijen, A.A., Martens, P.C.H.: 1989, *Astrophys. J.* **343**, 971. DOI: 10.1086/167766
- Battaglia, M., Kontar, E.P.: 2012, *Astrophys. J.* **760**, 142. DOI: 10.1088/0004-637X/760/2/142
- Biesecker, D.A., Myers, D.C., Thompson, B.J., Hammer, D.M., Vourlidas, A.: 2002, *Astrophys. J.* **569**, 1009. DOI: 10.1086/339402
- Bougeret, J.L., Goetz, K., Kaiser, M.L., Bale, S.D., Kellogg, P.J., Maksimovic, M., Monge, N., Monson, S.J., Astier, P.L., Davy, S. *et al.*: 2008, *Space Sci. Rev.* **136**, 487. DOI: 10.1007/s11214-007-9298-8



- Bougeret, J.-L., Kaiser, M.L., Kellogg, P.J., Manning, R., Goetz, K., Monson, S.J., Monge, N., Friel, L., Meetre, C.A., Perche, C., Sitruk, L., Hoang, S.: 1995, *Space Sci. Rev.* **71**, 231. DOI: 10.1007/BF00751331
- Brueckner, G.E., Howard, R.A., Koomen, M.J., Korendyke, C.M., Michels, D.J., Moses, J.D., *et al.*: 1995, *Solar Phys.* **162**, 357. DOI: 10.1007/BF00733434
- Carmichael, H.: 1964, *Proc. of AAS-NASA Symp. on the Physics of Solar Flares*, W. N. Hess, **NASA-SP 50**, 451.
- Chen, J.: 1989, *Astrophys. J.* **338**, 453. DOI: 10.1086/167211
- Chen, J.: 1996, *J. Geophys. Res.* **1012**, 27499. DOI: 10.1029/96JA02644
- Chen, P.F., Fang, C., Shibata, K.: 2005, *Astrophys. J.* **622**, 1202. DOI: 10.1086/428084
- Cheng, X., Zhang, J., Liu, Y., Ding, M.D.: 2011, *Astrophys. J. Lett.* **732**, L25. DOI: 10.1088/2041-8205/732/2/L25
- Cliver, E.W., Nitta, N.V., Thompson, B.J., Zhang, J.: 2004, *Solar Phys.* **225**, 105. DOI: 10.1007/s11207-004-3258-1
- Gallagher, P.T., Lawrence, G.R., Dennis, B.R.: 2003, *Astrophys. J. Lett.* **588**, L53. DOI: 10.1086/375504
- Gallagher, P.T., Long, D.M.: 2011, *Space Sci. Rev.* **158**, 365. DOI: 10.1007/s11214-010-9710-7
- Gopalswamy, N., Yashiro, S., Temmer, M. *et al.*: 2009a, *Astrophys. J. Lett.* **691**, L123. DOI: 10.1088/0004-637X/691/2/L123
- Gopalswamy, N., Thompson, W.T., Davila, J.M. *et al.*: 2009b, *Solar Phys.* **259**, 227. DOI: 10.1007/s11207-009-9382-1
- Gopalswamy, N., Yashiro, S., Michalek, G., Stenborg, G., Vourlidas, A., Freeland, S., Howard, R.: 2009c, *Earth, Moon, Planets* **104**, 295. DOI: 10.1007/s11038-008-9282-7
- Grechnev, V., Afanasyev, A., Uralov, A. *et al.*: 2011a, *Solar Phys.* **273**, 461. DOI: 10.1007/s11207-011-9781-y
- Grechnev, V.V., Kiselev, V.V., Uralov, A.M., Meshalkina, N.S., Kochanov, A.A.: 2013, *Publ. Astron. Soc. Japan* **65**, SP1, S9. DOI: 10.1093/pasj/65.sp1.S9
- Grechnev, V.V., Lesovoi, S.V., Smolkov, G.Y., Krissinel, B.B., Zandanov, V.G., Altyntsev, A.T., Kardapolova, N.N., Sergeev, R.Y., Uralov, A.M., Maksimov, V.P., Lubyshev, B.I.: 2003, *Solar Phys.* **216**, 239. DOI: 10.1023/A:1026153410061
- Grechnev, V., Uralov, A., Chertok, I., Kuzmenko, I.V., Afanasyev, A.N., Meshalkina, N.S., Kalashnikov, S.S., Kubo, Y.: 2011b, *Solar Phys.* **273**, 433. DOI: 10.1007/s11207-011-9780-z
- Grechnev, V.V., Uralov, A.M., Chertok, I.M., Slemzin, V.A., Filippov, B.P., Egorov, Ya.I., Fainshtein, V.G., Afanasyev, A.N., Prestage, N., Temmer, M.: 2014a, *Solar Phys.* **289**, 1279. DOI: 10.1007/s11207-013-0397-2
- Grechnev, V.V., Uralov, A.M., Slemzin, V.A., Chertok, I.M., Filippov, B.P., Rudenko, G.V., Temmer, M.: 2014b, *Solar Phys.* **289**, 289. DOI: 10.1007/s11207-013-0316-6
- Grechnev, V.V., Uralov, A.M., Slemzin, V.A., Chertok, I.M., Kuzmenko, I.V., Shibasaki, K.: 2008, *Solar Phys.* **253**, 263. DOI: 10.1007/s11207-008-9178-8
- Grechnev, V.V., Uralov, A.M., Zandanov, V.G., Baranov, N.Y., Shibasaki, K.: 2006, *Publ. Astron. Soc. Japan* **58**, 69. DOI: 10.1093/pasj/58.1.69
- Hanaoka, Y., Kurokawa, H., Enome, S., Nakajima, H., Shibasaki, K., Nishio, M., Takano, T., Torii, C., Sekiguchi, H., Kawashima, S., Bushimata, T., Shinohara, N., Irimajiri, Y., Koshiishi, H., Shiomi, Y., Nakai, Y., Funakoshi, Y., Kitai, R., Ishiura, K., Kimura, G.: 1994, *Publ. Astron. Soc. Japan* **46**, 205.
- Harra, L.K., Sterling, A.C.: 2001, *Astrophys. J. Lett.* **561**, L215. DOI: 10.1086/324767
- Hirayama, T.: 1974, *Solar Phys.* **34**, 323. DOI: 10.1007/BF00153671
- Howard, R.A., Moses, J.D., Vourlidas, A., Newmark, J.S., Socker, D.G., Plunkett, S.P., Korendyke, C.M., Cook, J.W. *et al.*: 2008, *Space Sci. Rev.* **136**, 67. DOI: 10.1007/s11214-008-9341-4
- Inhester, B., Birn, J., Hesse, M.: 1992, *Solar Phys.* **138**, 257. DOI: 10.1007/BF00151915
- Ji H., Wang H., Schmahl E.J., Moon Y.-J., Jiang Y.: 2003, *Astrophys. J. Lett.*, **595**, L135. DOI: 10.1086/378178
- Jin, M., Ding, M.D., Chen, P.F., Fang, C., Imada, S.: 2009, *Astrophys. J.* **702**, 27. DOI: 10.1088/0004-637X/702/1/27
- Kaiser, M.L., Kucera, T.A., Davila, J.M., St. Cyr, O.C., Guhathakurta, M., Christian, E.: 2008, *Space Sci. Rev.* **136**, 5. DOI: 10.1007/s11214-007-9277-0
- Kochanov, A., Anfinogentov, S., Prosovetsky, D., Rudenko, G., Grechnev, V.: 2013, *Publ. Astron. Soc. Japan* **65**, SP1, S19. DOI: 10.1093/pasj/65.sp1.S19
- Kopp, R.A., Pneuman, G.W.: 1976, *Solar Phys.* **50**, 85. DOI: 10.1007/BF00206193
- Krall, J., Chen, J., Santoro, R.: 2000, *Astrophys. J.* **539**, 964. DOI: 10.1086/309256

- Kumar, P., Cho, K.-S., Bong, S.-C., Park, S.-H., Kim, Y.H.: 2012, *Astrophys. J.* **746**, 67. DOI: 10.1088/0004-637X/746/1/67
- Kwon, R.-Y., Ofman, L., Olmedo, O., Kramar, M., Davila, J. M., Thompson, B.J., Cho, K.-S.: 2013, *Astrophys. J.*, **766**, 55. DOI: 10.1088/0004-637X/766/1/55
- Lemen, J.R., Title, A.M., Akin, D.J., Boerner, P.F., Chou, C., Drake, J.F., Duncan, D.W., Edwards, C.G., Friedlaender, F.M., Heyman, G.F. *et al.*: 2012, *Solar Phys.* **275**, 17. DOI: 10.1007/s11207-011-9776-8
- Lin, R.P., Dennis, B.R., Hurford, G.J., Smith, D.M., Zehnder, A., Harvey, P.R., *et al.*: 2002, *Solar Phys.* **210**, 3. DOI: 10.1023/A:1022428818870
- Longcope, D.W., Beveridge, C.: 2007, *Astrophys. J.* **669**, 621. DOI: 10.1086/521521
- Lynch, B.J., Antiochos, S.K., DeVore, C.R., Luhmann, J.G., Zurbuchen, T.H.: 2008, *Astrophys. J.* **683**, 1192. DOI: 10.1086/589738
- Ma, S., Raymond, J.C., Golub, L., Lin, J., Chen, H., Grigis, P., Testa, P., Long, D.: 2011, *Astrophys. J.* **738**, 160. DOI: 10.1088/0004-637X/738/2/160
- Mann, G., Klassen, A., Aurass, H., Classen, H.-T.: 2003, *Astron. Astrophys.* **400**, 329. DOI: 10.1051/0004-6361:20021593
- Martínez-Oliveros, J.-C., Hudson, H.S., Hurford, G.J., Krucker, S., Lin, R.P., Lindsey, C., Couvidat, S., Schou, J., Thompson, W.T.: 2012, *Astrophys. J. Lett.* **753**, L26. DOI: 10.1088/2041-8205/753/2/L26
- Meshalkina, N.S., Uralov, A.M., Grechnev, V.V., Altyntsev, A.T., Kashapova, L.K.: 2009, *Publ. Astron. Soc. Japan* **61**, 791. DOI: 10.1093/pasj/61.4.791
- Moore, R.L., Sterling, A.C., Hudson, H.S., Lemen, J.R.: 2001, *Astrophys. J.* **552**, 833. DOI: 10.1086/320559
- Nakajima, H., Nishio, M., Enome, S., Shibasaki, K., Takano, T., Hanaoka, Y., Torii, C., Sekiguchi, H. *et al.*: 1994, *Proc. IEEE* **82**, 705.
- Neupert, W.M.: 1968, *Astrophys. J. Lett.* **153**, L59. DOI: 10.1086/180220
- Parker, E.N.: 1961, *Astrophys. J.* **133**, 1014. DOI: 10.1086/147105
- Patsourakos, S., Vourlidas, A., Stenborg, G.: 2010, *Astrophys. J. Lett.* **724**, L188. DOI: 10.1088/2041-8205/724/2/L188
- Qiu, J., Hu, Q., Howard, T.A., Yurchyshyn, V.B.: 2007, *Astrophys. J.* **659**, 758. DOI: 10.1086/512060
- Reames, D.: 2009, *Astrophys. J.* **693**, 812. DOI: 10.1088/0004-637X/693/1/812
- Saito, K.: 1970, *Ann. Tokyo Astr. Obs.* **12**, 53.
- Sheeley, N.R., Hakala, W.N., Wang, Y.-M.: 2000, *J. Geophys. Res.* **105**, 5081. DOI: 10.1029/1999JA000338
- Sheeley, N.R., Jr., Warren, H.P., and Wang, Y.-M.: 2007, *Astrophys. J.* **671**, 926. DOI: 10.1086/522940
- Shimojo, M., Yokoyama, T., Asai, A., Nakajima, H., Shibasaki, K.: 2006, *Publ. Astron. Soc. Japan* **58**, 85. DOI: 10.1093/pasj/58.1.85
- Smerd, S.F., Sheridan, K.V., Stewart, R.T.: In Newkirk, G.A. (ed.) 1974, *Coronal Disturbances*, IAU Symp. 57, Springer, Netherlands, 389.
- Smolkov, G.I., Pistolkors, A.A., Treskov, T.A., Krissinel, B.B., Putilov, V.A.: 1986, *Astrophys. Spa. Sci.* **119**, 1. DOI: 10.1007/BF00648801
- Sterling, A.C., Moore, R.L., Thompson, B.J.: 2001, *Astrophys. J. Lett.* **561**, L219. DOI: 10.1086/324765
- Sturrock, P.A.: 1966, *Nature* **211**, 695. DOI: 10.1038/211695a0
- Sui, L., Holman, G.D., Dennis, B.R.: 2008, *Adv. Space Res.* **41**, 976. DOI: 10.1016/j.asr.2007.03.031
- Temmer, M., Veronig, A.M., Vršnak, Rybák, J., Gömöry, J., Stoiser, S., Maričić, D.: 2008, *Astrophys. J. Lett.* **673**, L95. DOI: 10.1086/527414
- Temmer M., Veronig, A.M., Kontar, E.P., Krucker, S., Vršnak, B.: 2010, *Astrophys. J.* **712**, 1410. DOI: 10.1088/0004-637X/712/2/1410
- Thompson, B.J., Gurman, J.B., Neupert, W.M., Newmark, J.S., Delaboudinière, J.-P., St. Cyr, O.C., Stezelberger, S., Dere, K.P., Howard, R.A., Michels, D.J.: 1999, *Astrophys. J. Lett.* **517**, L151. DOI: 10.1086/312030
- Uchida, Y.: 1968, *Solar Phys.* **4**, 30. DOI: 10.1007/BF00146996
- Uralov, A.M.: 1990a, *Solar Phys.* **127**, 253. DOI: 10.1007/BF00152165
- Uralov, A.M.: 1990b, *Washington DC American Geophysical Union Geophysical Monograph Series* **58**, 285.
- Uralov, A.M., Grechnev, V.V., Rudenko, G.V., Myshyakov, I.I., Chertok, I.M., Filippov, B.P., Slemzin, V.A.: 2014, *Solar Phys.* **289**, 3747. DOI: 10.1007/s11207-014-0536-4

- Uralov, A.M., Lesovoi, S.V., Zandanov, V.G., Grechnev, V.V.: 2002, *Solar Phys.* **208**, 69. DOI: 10.1023/A:1019610614255
- Uralova, S.V., Uralov, A.M.: 1994, *Solar Phys.* **152**, 457. DOI: 10.1007/BF00680450
- Vourlidas, A., Wu, S.T., Wang, A.H. *et al.*: 2003, *Astrophys. J.* **598**, 1392. DOI: 10.1086/379098
- Vršnak, B., Cliver, E.W.: 2008, *Solar Phys.* **253**, 215. DOI: 10.1007/s11207-008-9241-5
- Vršnak, B., Gopalswamy, N.: 2002, *J. Geophys. Res.* **107**, A1019. DOI: 10.1029/2001JA000120
- Vršnak, B., Maričić, D., Stanger, A.L., Veronig, A.M., Temmer, M., Roša, D.: 2007, *Solar Phys.* **241**, 85. DOI: 10.1007/s11207-006-0290-3
- Wang, Y., Zhang, J., Shen, C.: 2009, *J. Geophys. Res.* **114**, A10104. DOI: 10.1029/2009JA014360
- Wills-Davey, M.J., Attrill, G.D.R.: 2009, *Space Sci. Rev.* **149**, 325. DOI: 10.1007/s11214-009-9612-8
- Yashiro, S., Gopalswamy, N., Michalek, G., St. Cyr, O.C., Plunkett, S.P., Rich, N.B., Howard, R.A.: 2004, *J. Geophys. Res.* **109**, A07105. DOI: 10.1029/2003JA010282
- Zhang, J., Dere, K.P., Howard, R.A., Kundu, M.R., White, S.M.: 2001, *Astrophys. J.* **559**, 452. DOI: 10.1086/322405

